Emerging Applications in Tokamak Plasma Control

CONTROL SOLUTIONS FOR NEXT-GENERATION TOKAMAKS

MICHAEL L. WALKER, DAVID A. HUMPHREYS, DIDIER MAZON,
DIDIER MOREAU, MICHIO OKABAYASHI, THOMAS H. OSBORNE, and EUGENIO SCHUSTER

Solutions for many tokamak control problems are important for continuing progress toward producing energy from fusion. Areas of development include basic physics, development and modeling of actuators and sensors for control, experimental use of initial simple controllers, and the development of sophisticated control algorithms. In this article, we review several tokamak plasma control problems and describe progress achieved at tokamak devices around the world.

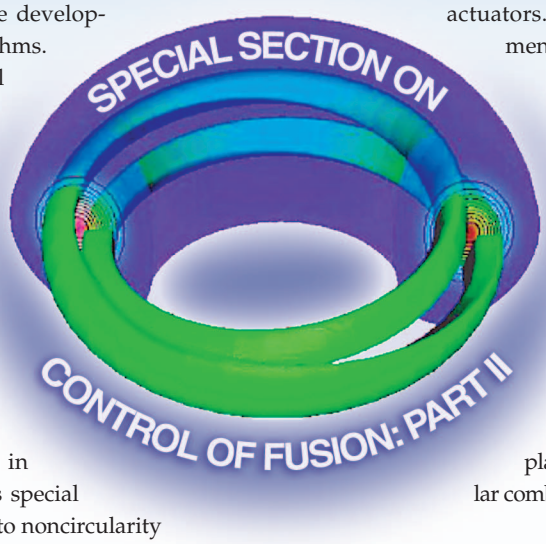

A practical tokamak fusion reactor must operate at high temperature, high pressure, and high current. These tokamak plasmas are susceptible to numerous instabilities, some of which pose a risk to the device itself (see "Tutorial 18" in [1]). An example seen earlier in this special section is the vertical instability due to noncircularity of the plasma ("Tutorial 14" in [1]). The vertical instability is axisymmetric, that is, the plasma motion is the same at all toroidal angles and is characterized by a primarily vertical displacement. Increases in growth rates of the vertical instability and of other plasma instabilities correspond to increases in plasma pressure. Consequently, the most attractive operational regimes from the perspective of a fusion power reactor tend to be those that are nearest to instability.

In this article, we describe three different plasma instabilities and the control approaches for their stabilization. The objective of stabilization is to prevent loss of the plasma while retaining high performance; in fact, pushing the plasma into higher-performance regimes is often what triggers a particular instability. Stabilization algorithms are initially based on ideal magnetohydrodynamic (MHD) models ("Tutorial 3" in [2]), while more accurate extensions of these models are used to account for additional effects.

In addition to mode stabilization, off-normal events must be "handled" rather than controlled in the sense of feedback. These events, which occur due to occasional loss of control, include instabilities that are uncontrollable with present actuators. Efforts have been made on experimental devices to define and implement responses to some of these events. We describe examples of off-normal events as well as relevant control methods.

Additional control problems include control of internal plasma parameters, such as the current, temperature, and density profiles ("Tutorial 5" in [2]), and control of transport, that is, the continuous flow of particles, heat, and current, in the plasma interior. We describe one particular combination of this class of problems.

SUPPRESSION OF THE NEOCLASSICAL TEARING MODE

Increasing beta ("Tutorial 2" in [2]) in a resistive plasma can make the nested magnetic surface topology required by ideal MHD (Figure C in "Tutorial 1" in [2]) unstable, resulting in tearing and reconnection of the flux surfaces. When this reconnection occurs, a structure called a magnetic island is formed (Figure 1). The instability known as a neoclassical tearing mode (NTM) drives an island to a maximum size defined by the underlying nonlinear physics, which then persists stably in the plasma [3]. The island winds helically around the tokamak with a helicity given by the value of the safety factor q ("Tutorial 4" in [2]) on the surface where it forms. The NTM forms on flux surfaces whose safety factor is q rational, the most important of which are the $q = 3/2 = 1.5$ or the $q = 2/1 = 2.0$ surfaces. The 2/1 NTM often produces a plasma-terminating disruption ("Tutorial 18" in [1]) by triggering an ideal MHD

CREDIT: DYLAN BRENNAN, GENERAL ATOMICS, & NIMROD PROJECT

1066-033X/06/$20.00©2006IEEE

A Guide for the Reader

This article discusses several tokamak control problems, each of which requires an understanding of some basic plasma physics. We rely on the introductory paper [2] as well as the numbered tutorials in the previous installment of this special section. In most cases, the introductory paper or a tutorial is cited to help the reader locate a term or concept. In [2], there is a list of plasma physics terms and the locations where each term is defined. Each section of the present article discusses a separate control problem, and each section can be read independently of all other sections. The separate topics are ordered according to the level of physics background needed to understand them.

mode, which can grow to be comparable in size to the plasma cross section, while the 3/2 NTM usually remains small enough to merely degrade confinement. The presence of the island can degrade confinement by connecting hotter inner regions of the plasma to colder outer regions with "short circuiting" magnetic field lines, allowing heat to leak out of the plasma core faster than it would without the island. The resulting flattening in temperature, pressure, and current profiles ("Tutorial 5" in [2]) across the island (Figure 2) corresponds to a steady-state lowering of total plasma internal energy and therefore an overall colder, less efficient plasma.

In most cases, the NTM requires a triggering instability such as an edge localized mode [(ELM) see later section on ELMs] to produce a seed island, which grows when the NTM is unstable [4]. One way to control the NTM is, therefore, to ensure that triggering instabilities do not occur. Unfortunately, experimental evidence suggests that NTMs can also be triggered by background plasma turbulence, which is difficult or impossible to completely eliminate [5]. For this reason, eliminating events that can produce a seed island may not suffice to control NTMs. An alternative method for controlling NTMs using auxiliary current drive has been successfully demonstrated on several tokamaks. This approach replaces the current lost in the process of flattening the profiles across the island. The restoration of current shrinks the island, restores the nested flux surface magnetic topology [Figure 1(a)], and stabilizes the mode [6]. In addition to local control of the current profile, global control might also prevent NTMs. Global control of current profiles is described in a later section on profile control.

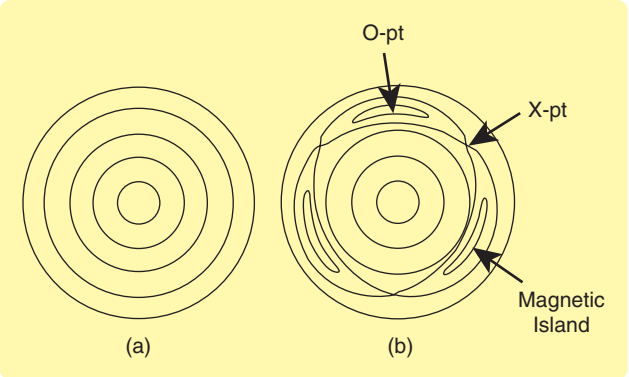

FIGURE 1 Magnetic island topology in a circular cross-section plasma. (a) Perfectly conducting ideal MHD plasmas (Tutorial 3 in [1]) require nested flux surfaces, (b) while resistive plasmas can produce tearing and *reconnection* (hence the name *tearing mode*) of flux surfaces, resulting in magnetic islands. The current and pressure profiles (Tutorial 5 in [1]) are flattened across an island, whose center is the *O-point*. The resulting connection between inner and outer island surfaces, joined at the *X-point*, allows heat to leak out of the plasma core faster than it would without the island, thus degrading confinement. (b) shows the island topology corresponding to a 3/2 NTM, which has a periodicity of $m = 3$ (Tutorial 4 in [1]) in the poloidal cross section shown and a periodicity of $n = 2$ in the toroidal direction (not illustrated).

Stabilization by Injection of Current

Using a variety of methods, current can be driven at the flux surface that contains islands. Electron cyclotron current drive (ECCD) (see "Tutorial 9" in [7]) can produce highly localized current drive and has been successful in stabilizing the NTM [8]. ECCD drives current in regions typically a few centimeters wide by injecting microwave frequency electromagnetic waves that resonate with the cyclotron orbits (Figure 8 in [2]) of the current-carrying plasma electrons. In tokamaks, these waves are usually produced by high-power gyrotrons, similar to the wave generators used in satellite communications. Since the electron cyclotron frequency depends primarily on the local toroidal magnetic field, the current is driven where the injected wave path intersects the radial location at which the waves are resonant. Figure 3 illustrates this geometry in a DIII-D tokamak [2] discharge. The injection chord is not straight, owing to refractive effects of the plasma. For large tokamaks operating today, such as JET, DIII-D, and ASDEX-U, injected power on the order of a few megawatts is required to produce the tens of kiloamps of plasma current needed to stabilize the mode [6].

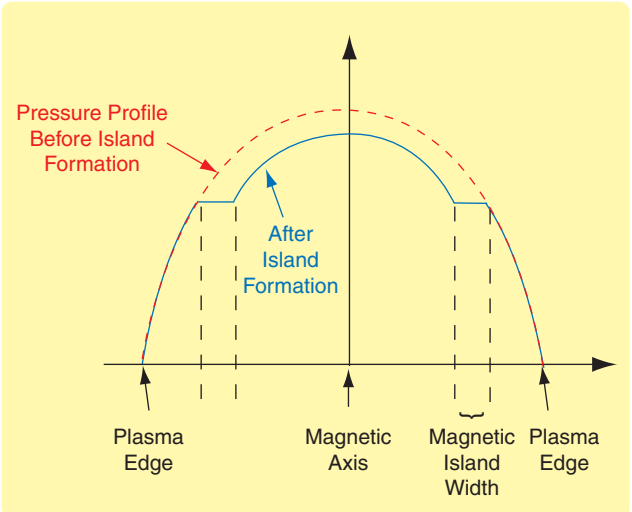

FIGURE 2 Flattening of the pressure profile caused by the NTM. Islands driven by the NTM are responsible for decreasing the temperature, pressure, and current inside the island.

For islands that are a few centimeters wide, the alignment of island and deposition locations must be accomplished with accuracy on the order of a centimeter. The deposition need only lie on the flux surface containing the NTM islands, rather than directly threading the center of each helical island itself. However, driving current only within the islands, and not outside, would reduce the power required to stabilize the mode.

The timescale for ECCD-driven current to rise in a present-day tokamak is tens of milliseconds. This time is comparable to the time required for the island to grow to a saturated state or to respond to the current drive and reduce in size when the deposition region is sufficiently aligned with the island flux surface to produce suppression. Several mechanisms are available to perform a sufficiently fast alignment . One approach is to vary the wave launcher mirror angle, which in turn varies the angle of the injection wave path (Figure 3) [9]. This method has the advantage of leaving the plasma equilibrium characteristics unchanged. Another approach is to vary the toroidal field. This approach moves the radial location of the harmonic resonance, and thus the deposition location, back and forth relative to the island (see Figure 3). Toroidal field variation leaves the plasma shape and position unchanged, allowing divertor pumping ("Tutorial 6" in [7]) and stability characteristics that depend on the shape to be held constant. This approach has been used in stabilizing both 3/2 and 2/1 NTMs [11].

Still another approach involves moving the plasma, and thus the island, position relative to the approximately fixed deposition location. Although moving the plasma radially can be accomplished with approximately constant divertor pumping and plasma shape, moving the plasma vertically tends to significantly affect the divertor configuration, although with little effect on the shape. Nevertheless, while modifying the toroidal field requires on the order of 100 ms or more owing to the large L/R time of toroidal field (TF) coils, varying the plasma position requires <10 ms. This speed advantage means that plasma position control can produce adequate alignment in a shorter time, and thus phase lags in the control action and island response are significantly reduced. Launcher angle control can, in principle, be comparable in speed to plasma position control.

Algorithms for Controlling the Current Deposition

The central problem in using these methods to align the current drive deposition and island locations is difficulty in determining the location of the island flux surface and the deposition location in real time. Present-day diagnostics and equilibrium reconstructions (see [7]) produce estimates of the island flux surface location with typical accuracy of ± 1–± 1.5 cm, comparable to the accuracy with which island positioning can be accomplished by modifying the plasma position or toroidal field. In addition, more accurate determination of the deposition location requires complex computations that at present cannot be accomplished in real time. To overcome this difficulty, a suite of search and tracking algorithms has been developed on DIII-D to address these issues and produce successful, sustained NTM suppression. In particular, the DIII-D NTM control system uses three coupled algorithms: the search and suppress, active tracking, and target lock routines. Each algorithm can affect any of three different island/ECCD alignment control variables, specifically, the plasma major radius position (Figure A in "Tutorial 1" in [2]), the toroidal field, or the plasma vertical position.

The operation mode most successfully and routinely applied to date combines search and suppress with active tracking (Figure 4). When the control is enabled, the algorithm fixes the selected control variable for a specified dwell time to determine whether the degree of alignment is sufficient to suppress the mode. If, at the end of this dwell time, the mode amplitude has been reduced at a sufficiently high rate relative to a specified threshold rate or has fallen below a specified threshold amplitude, the algorithm continues to hold the control variable fixed. Otherwise, the algorithm executes a search by incrementing the control variable by a specified amount, freezing that variable for another dwell time, and examining the resulting effect on the mode. The search/dwell/search sequence continues until suppression is

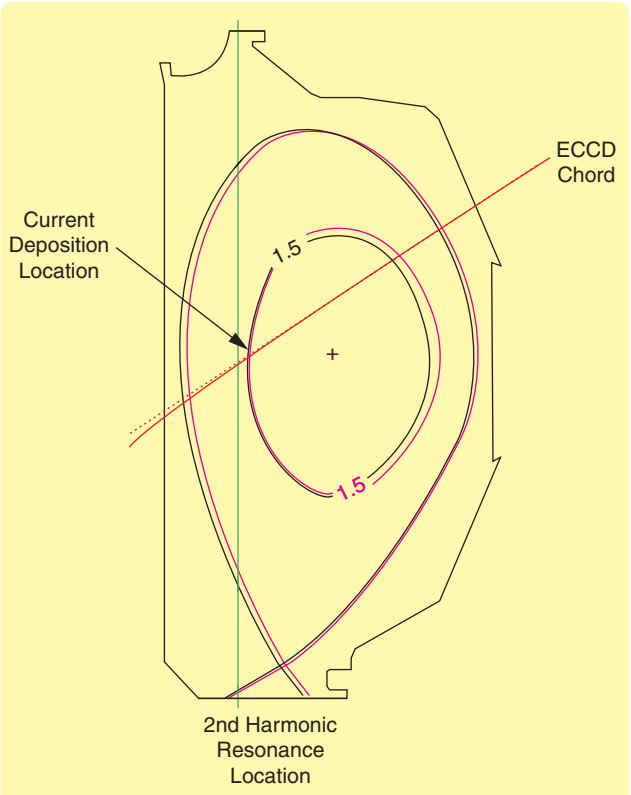

FIGURE 3 Geometry of current drive to suppress NTM islands. Driving current with ECCD at the flux surface that contains islands can restore the current lost in island formation. This extra current shrinks and can even eliminate the island, thus stabilizing the mode. The affected flux surface shown, for two different times during the discharge, corresponds to the 3/2 NTM and is labeled by the safety factor contour value of 1.5. The location where current is actually deposited is slightly offset from the electron cyclotron second harmonic resonance due to a Doppler shift.

achieved or a specified limit in the control variable is reached, in which case the search reverses the sign of the control variable increment. This process continues until sufficient alignment is detected and the mode is suppressed below the specified amplitude threshold.

Once sufficient alignment is detected, the control variable is frozen and the active tracking algorithm is engaged. The active tracking algorithm adjusts the control variable to maintain alignment while the detected mode amplitude is below the specified threshold. The required adjustment is determined by real-time equilibrium and q-profile reconstruction using measurements of the internal magnetic topology with motional Stark effect (MSE) sensors [12]. The MSE sensors measure the local ratio of poloidal and toroidal magnetic fields at a set of discrete points within the plasma. If internal measurements are not available, linear or nonlinear estimators based on magnetic measurements are used, including neural-network-based algorithms. These estimators are trained on previous experimental discharge data or artificially generated data to estimate the position of the relevant q-surface. The adjustment to the control variable required to maintain alignment is derived from the difference between the q-surface position estimate and the ECCD deposition location. While neural network predictors have been successfully applied in DIII-D, flux surface reconstruction based on direct magnetic measurements provides the most accurate and reliable sustained alignment.

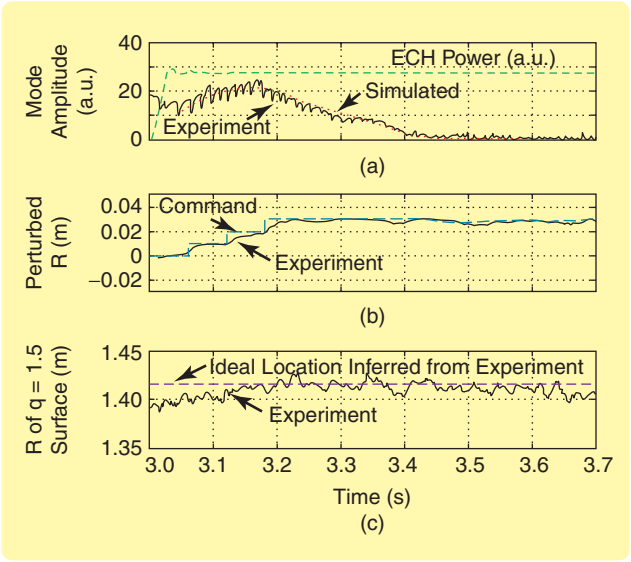

FIGURE 4 The DIII-D search and suppress algorithm with active tracking. The figure illustrates the successful use of this method for suppressing the NTM and sustaining stabilization during DIII-D plasma discharge 115267. The search and suppress algorithm is engaged at approximately 3.0 s, while active tracking is engaged at approximately 3.4 s. (a) The experimental NTM mode amplitude, which varies with the island width, is well predicted by the NTM model. This plot also shows the input ECH power. The notation a.u. (arbitrary units) indicates that no effort has been made to convert the signal to standard units such as meters or MW. (b) The plasma major radius is modified to achieve and maintain alignment between the NTM island and ECCD deposition locations. (c) The radial location corresponding to the peak of ECCD current deposition is determined empirically after the discharge. The control during the discharge causes the radius of the 3/2 NTM island flux surface to be nearly optimally aligned with this location.

The design of the parameters governing the search and suppress and active tracking algorithms is accomplished using accurate dynamic models of both the NTM island response to ECCD and the plasma response to position commands. Figure 4(a) shows a comparison of model-predicted and experimental responses when alignment between the NTM island and ECCD location is varied. The model response, based on a simplified version of the modified Rutherford equation that describes island dynamics, shows sufficiently accurate representation of island response to allow for good control design [6]. In the case shown, the plasma major radius (middle frame) is varied to adjust the alignment of the $q = 1.5$ surface with the ECCD deposition location. The NTM control algorithm is integrated with a special plasma shape and position regulation scheme that fixes the strike points (Figure C in "Tutorial 1" in [2]) while varying the major radius. Fixing the strike points allows for constant divertor pumping while NTM suppression is performed. Following suppression of the mode, where it is assumed that deposition is aligned with the $q = 3/2$ surface, the active tracking algorithm is enabled to compensate for variations in the $q = 1.5$ surface due to changes in the current profile and poloidal beta. The active tracking action can be seen in the fluctuating perturbations of the $q = 3/2$ radius following suppression at $t \approx 3.4$ s.

In the experiment shown in Figure 4, the growth of the mode is slowed even when the island and ECCD are misaligned by as much as 1.5–2 cm. Adjustment of the major radius by the search and suppress algorithm produces sufficient alignment to fully suppress the mode within 200 ms after alignment is attained. After design and testing of the basic scheme, proper functioning of the algorithm requires specification of various parameters and thresholds to match the dynamic characteristics of the target equilibrium. Dynamic models of NTM response are sufficiently reliable such that, the first time this integrated active suppression was attempted experimentally, the control algorithm with parameters tuned using these models successfully suppressed the NTM and tracked the evolution of the profile, thereby maintaining ECCD alignment with the island [6].

An alternative to the search and suppress algorithm is the target lock algorithm. This control scheme uses the observed response of the mode amplitude to either natural fluctuations or preprogrammed variations in the control variable to infer the proximity to ideal alignment. An approximate form of the modified Rutherford equation [6] is implemented in this algorithm to estimate the expected mode decay or growth rate based on the degree of misalignment.

The search and suppress, active tracking, and target lock algorithms enable full and sustained suppression of both 3/2 and 2/1 NTMs in DIII-D under closed-loop control. Suppression of the 3/2 NTM allows operation at normalized beta values of

around 3.4, approximately 50% above the $\beta_N = 2.3$ value achieved in the presence of the unsuppressed mode [6]. The duration of increased-beta operation is limited only by the length of time that the gyrotrons can inject power into the plasma.

Eventual application of NTM suppression to fusion reactors envisions several possible modes of operation. In one scenario, current drive is applied in steady state at the relevant flux surfaces to preemptively suppress seed islands that might be triggered by background MHD instabilities or turbulence. Because the current drive source must operate constantly in this scenario, a large amount of auxiliary power is required. This approach also requires constant tracking of the ECCD deposition location and target flux surfaces to maintain alignment. Another approach to NTM suppression is to detect the presence of NTM islands and suppress the mode as rapidly as possible, before a 2/1 island reaches a potentially disruptive saturated size or a 3/2 island significantly degrades confinement. This method demands a rapid island acquisition and alignment system to suppress the NTM within tens of milliseconds after the onset of island growth. Of course, continuous calculation of the flux surface geometry and computation of the expected deposition location can allow the system to be engaged quickly and thus meet this suppression time requirement. Gyrotrons, for example, can be ramped to full power in significantly less than 10 ms.

Future Directions

It is widely accepted that localized current drive can replace the missing current that characterizes the NTM, thereby stabilizing the mode. Closed-loop feedback approaches have demonstrated NTM suppression sustained for several seconds on various tokamaks. However, before current drive suppression can be used effectively in a reactor-grade plasma, several key capabilities must be demonstrated. The principal requirement in a reactor is reliable, simultaneous, and steady-state suppression of both the 3/2 mode, which mainly degrades confinement, and the 2/1 mode, which can lead to a disruption. Demonstrating simultaneous stabilization requires more installed current drive power than is presently available in any machine, independently steerable launchers, more accurate and reliable real-time reconstruction of internal magnetic surfaces, accurate real-time determination of the current deposition location, and algorithms that can deal with changing equilibrium and machine conditions.

Work has begun on installing steerable launchers in several tokamaks, and real-time steering has been demonstrated in JT-60U. Although real-time magnetic surface reconstruction has been demonstrated in DIII-D, improved levels of accuracy are required to sustain suppression for the longer 10-s pulses expected in the 2006–2007 campaigns. Algorithms for detecting the location of optimal alignment and maintaining alignment once the mode is suppressed have also been developed, but leave room for improvement. While NTM suppression in tokamaks is evolving, the objective can benefit from advances in control algorithms, estimation, real-time computation, actuator technology, and diagnostic signal interpretation.

DETECTION, CORRECTION, AND MITIGATION OF OFF-NORMAL EVENTS

By definition, off-normal events do not usually occur during well-controlled steady-state operation. The impact of off-normal events in a tokamak can be summarized according to the severity of their consequences.

1) Risk of personnel safety. These events can cause harm to operating personnel or the general public. A categorization of off-normal events from a safety point of view is given in [13].
2) Risk of equipment safety. These events can cause damage to either the device or the facility but do not risk the safety of personnel.
3) Performance degradation. These events can cause the performance of tokamak operation to degrade but do not create risk to either personnel or equipment.

The primary personnel risks at a tokamak facility are due to the high currents and voltages used to confine and heat the plasma, radiation from activated materials or tritium release, and conventional process control risks such as toxic chemicals, high pressures, or extremely high or low temperatures. Most of the approaches for dealing with these risks are rather conventional and are already in use at major facilities. The main risks to the device or facility derive from the large energy content in the plasma while the tokamak is operating. Off-normal events that lead to plasma termination, such as major disruptions ("Tutorial 18" in [1]), can deposit a significant amount of energy onto plasma-facing components or create large and potentially damaging mechanical forces.

The handling of off-normal events includes detection and identification of the off-normal event, determination and execution of corrective action, and execution of a mitigating response when correction or recovery is not possible. In future power-producing reactors, the system responsible for off-normal event detection and response must be seamlessly integrated with the multiple plasma control subsystems as well as the overall machine and safety supervisory system.

Responses to off-normal events generally depend on the risk associated with the event. A fast plasma termination is initiated if an event poses an imminent threat to personnel, the device, or the facility. However, a fast plasma termination can cause structural damage by localized deposition of thermal or magnetic energy. Mitigating these effects requires termination techniques that homogeneously distribute the plasma energy. A controlled plasma termination is initiated when continued operation could lead to a potential risk. In present devices, discharges are usually not terminated for reasons of reduced performance. Efforts are made, however, to recover from the performance reducing event, either in the same discharge or in those that follow.

A fast plasma termination can also be an unintended consequence of a control failure. A loss of controllability can originate in the failure of a component or subsystem of a feedback loop, in the operation of the system at operating points for which the controller is not designed, or at operating conditions that trigger other types of instabilities.

In the following subsections, we describe methods for handling disruptions, system fault detection and isolation, and performance optimization. The problems described are examples of a broad collection of off-normal events that must be handled in real time to enable a viable power-producing fusion reactor.

Disruption Avoidance and Mitigation

Erosion due to disruption reduces the lifetime of plasma-facing components. Sometimes, long-term reconditioning of plasma-facing surfaces after disruptions is required before normal plasma operation can be resumed. It is therefore desirable to avoid disruptions and to reduce their effects. Approaches to disruption avoidance can be divided into two categories [14]: 1) avoidance of the operating conditions that lead to disruption and 2) intervention after real-time prediction of disruption onset.

By ensuring that the plasma stays within a disruption-free scenario ("Tutorial 13" in [10]), it is possible to avoid the operational limits and conditions that cause disruptions. However, optimizing plasma performance often requires operating near disruption limits. Disruption-free scenarios are often based on conservative plasma operation parameters that do not come close to known disruption-initiating or plasma control limits.

In cases where disruption avoidance procedures operate close to allowable limits, observation of the limits involved and real-time disruption prediction or onset warning capability become important. Basing disruption prediction on proximity to a single parameter limit or the confluence of several single parameter limits may not provide complete certainty for disruption avoidance and can restrict the accessible operation domain. An improvement can be made by implementing a nonlinear multivariable disruption predictor, wherein multiple disruption-related indicators or diagnostic signals are combined to provide a composite disruption warning indicator that is more robust and reliable than simple single- or multiple-parameter indicators. For example, after training, neural networks are able to predict disruptions in DIII-D [15] and classify disruptions in JET [16]. Enhanced prediction capabilities (85%) are achieved in ASDEX-U using a neural network disruption predictor [17]. More complex systems [18] are capable of disruption prediction with a probability of 95%.

Ideally, an impending disruptive MHD instability can be detected and avoided by modifying the target equilibrium, heating, density, or other operating parameters. If avoidance is not possible, mitigation of its effects is required. Plasma facing component damage is primarily due to an excessive surface temperature rise leading to melting or ablation, which cannot be ameliorated by improving the heat removal capability of the plasma-facing component heat sink. Effective thermal mitigation approaches involve maximizing the time during which the energy is released or expanding the region over which the energy is deposited. This goal can be achieved by the fast injection of impurities. Ultraviolet radiation from the injected impurities distributes the plasma energy more uniformly on the first wall, reducing the thermal load in any one location. The most effective methods are solid pellet injection [19] and intense gas puffing [20].

Fault Detection and Isolation

During tokamak operation, hundreds of subsystems must operate correctly and simultaneously for a successful plasma discharge. Verifying proper operation of the subsystems most prone to failure is often done manually by human operators after the discharge. Because of the tedious nature of this task and the large number of systems, inoperative or malfunctioning systems can remain undetected until several experimental discharges have passed. Occasionally, problems are not detected until days later, especially if the failure does not prevent operation. Efforts are being made toward developing automated fault detection systems [21]–[23].

Fault detection and isolation (FDI) techniques have been under development for the last three decades. In hardware redundancy methods [24], multiple physical subsystems, such as multiple sensors, are installed and their output signals are compared for consistency. In the event of failure, a subsystem backup is switched in. Characteristics of this approach are high cost, additional space requirements, and hardware complexity. In analytic redundancy methods, the inherent redundancy contained in the static and dynamic relationships among the inputs and outputs of the system, for example, systems in which there are more measurements than independent states, is exploited. The measurements of the system inputs and outputs are processed analytically to obtain estimates for evaluating the condition of the system. These estimates can be generated using either quantitative or qualitative models.

For quantitative, that is, mathematical, models, the model-based predictors are state estimation, parameter identification, and parity space methods. For qualitative, nonmathematical models, the prediction is based on decision-table-based methods, knowledge-based expert systems, and neural-network-based methods. The estimated variable is compared with the corresponding measured value of the variable to generate a residual. Deviations of this residual that indicate a failure are detected by methods such as Bayes decision and hypothesis testing.

Due to the complexity of tokamak systems and the number of variables to be monitored, current efforts toward FDI are based primarily on qualitative approaches. Each type of fault is characterized by a specific combination of symptoms. Classification methods such as fuzzy clustering, artificial neural networks, and geometrical distance are used to determine the type of fault [25]. If more information about the relations between symptoms and faults is available in the form of diagnostic models, methods of reasoning can be applied. The reasoning strategies for fault diagnosis are probabilistic reasoning, rule-based reasoning, sign-directed graph, fault symptom tree, and fuzzy logic.

Examples of Fault Detection in Present Tokamaks

At JET, an automatic modular sensor fault detection and classification [21] system has been built for the sensors measuring the vertical mechanical stresses on the supports of the vacuum

Power systems for tokamak control problems are a challenge due to simultaneous requirements for high voltages and currents and speed of response.

vessel of the tokamak. Experts are interested in the reliability of these measurements during specific time windows corresponding to the occurrence of disruptions. During the usual operational life of the tokamak, in fact, mechanical stresses are weak and do not need to be monitored. However, fast dynamic vertical displacement events (VDEs, see "Tutorial 18" in [1]) cause an impulsive force and mechanical oscillations of the vacuum vessel, which must be monitored to ensure mechanical integrity of the tokamak. One of the actions related to the mechanical monitoring of the stresses is to suspend the experimental campaign when more than a fixed number of VDEs trespass a certain stress threshold in a day. The reliability of the measurements is therefore important for avoiding both unwarranted suspension of the experiments and dangerous experiments carried out above the operational limits. The strategy used at JET is based on a modular system that consists of two stages. The first stage is a multilayer perceptron neural network that predicts features of the signals on the basis of selected inputs [22]. The predicted features are compared with the actual feature values, and alarms are raised indicating sensor faults if the corresponding residuals are too high. This task is part of the fault detection phase, which consists of revealing the presence of a fault. The second stage focuses on fault classification, which is accomplished by a fuzzy inference system. In this case, the fault classification rules are established on the basis of manual fault classification previously performed by experts. The tuning of the membership functions is set by trial and error, taking into account sensor accuracy and disturbance level.

An expert-system-based fault detection system used routinely during DIII-D operations has increased tokamak productivity. The fault identification and communication system (FICS) [23] executes automatically after every plasma discharge to evaluate dozens of device subsystems for proper operation and communicate the results to the tokamak operator. The two primary purposes of FICS are fault detection and fault prediction. Fault detection refers to determining which systems are not working properly during an experiment, even if there is no loss of experimental discharge. Fault prediction refers to determining which systems appear to be having trouble and may cause a future fault. This process includes detecting programming errors, that is, determining whether the operator specified setup for a discharge is self-consistent.

The core of FICS uses the public domain C language integrated production system (CLIPS) software, a computer language designed for implementing expert systems. Originally developed by NASA [26], CLIPS provides two powerful capabilities not available in conventional programming languages. Chaining provides the ability to emulate a human chain of reasoning in software. Data-driven execution enables the expert-defined rules to activate as soon as a knowledge or data source becomes available. The CLIPS shell performs the inferences, executing rules of the form "if A, then B." In its simplest form, CLIPS consists of facts and rules. Rules are executed when specified facts are asserted, for example, "A" in the clause "if A, then B." The consequences of a rule execution are to assert other facts "B," which can then execute other rules. An important side effect of rule execution is the ability to activate functions that extract and manipulate data and return the results of those manipulations to the expert system. This information can then be used to assert more facts to drive other rules. The order of rule execution can be influenced by a priority value assigned to each rule. Rules are executed according to their relative priority and according to when their data become available. Since the program is data driven, each rule executes if and when the data is acquired. If a particular piece of data is not available, tests that require this data do not execute, and an alarm is raised indicating that the required data were not acquired.

The success of a fault detection system depends on the availability of measured data. Present devices can acquire a huge amount of experimental data, up to several gigabytes per discharge of only a few seconds duration. Steady state operation will place significant new demands on data storage, even with slow data acquisition rates. On the other hand, the data acquisition system must be able to capture rapid and unpredictable changes for use in fault detection and identification. For this purpose, new data acquisition methods developed for the TRIAM-1M [27] and JET [28] tokamaks combine coarse data from quiescent steady-state phases with fine data from rapid and unpredictable transitions. In future steady-state tokamaks, such finely sampled data will be used to detect and respond to off-normal events.

Performance Optimization Through Event Handling

Catastrophic loss of plasma or failure of tokamak systems are the most obvious off-normal events. Other, more subtle events, one of which is described below, simply degrade performance. Thus, methods to handle and correct these events can be thought of as performance optimization. A good example of performance optimization is the detection and handling of the H-mode to L-mode ("Tutorial 19") back-transition that occurs in ASDEX-U [29]. The performance control in ASDEX-U is dedicated to the control of plasma characteristics such as confinement or radiative behavior, which are rather weakly coupled to parameters related to, for example, the plasma

Tutorial 19: Confinement Modes

The energy confinement time τ_E ("Tutorial 2" in [2]) is an important measure of the ability of a plasma to retain energy and thereby support continuing fusion reactions. In the tokamak experimental community, plasma confinement properties are categorized as one of four confinement modes. The first of these modes is the ohmic plasma, which is heated only by the ohmic transformer action ("Tutorial 9" in [7]). The three remaining modes use methods of auxiliary heating as well as ohmic heating. In order of increased confinement, these three modes are the low-confinement mode or L-mode, the high-confinement mode or H-mode, and several versions of very-high-confinement modes. These modes are primarily distinguished by the shape of their temperature, pressure, and density profiles ("Tutorial 5" in [2]) with the higher confinement modes exhibiting steeper gradients. The terms ohmic plasma, L-mode, and H-mode have become more or less accepted terminology, while the terms describing the highest confinement regimes vary between institutions.

H-mode [31] is the target regime for the advanced tokamak concept (see [2]), since higher-confinement modes have only been produced transiently and have always been terminated by a severe MHD instability.

position and shape control. Several process controllers, usually simple single-variable proportional-integral controllers, are used to control different characteristics of the plasma, including various forms of density, temperature, and pressure, as well as fueling mixtures and power flows. These basic process controllers are combined to define control recipes, which are switched on and off during the discharge. Activation of the control recipes at preset times during the discharge to optimize a plasma characteristic is not practical because it is difficult, if not impossible, to predict the conditions of the plasma. A real-time algorithm for plasma-regime recognition [29] is therefore used as the trigger mechanism for the control recipes. The first version identifies five confinement regimes ("Tutorial 19"): the ohmic phase (OH), standard L-mode (L), standard H-mode (H), highly radiating L-mode (HRL), and highly radiating H-mode (HRH). This algorithm allows the switching of control recipes to recover plasma performance. For example, the working point for best HRH plasma performance is close to the H-mode to L-Mode back transition, so that occasional back transitions occur. When they do occur, the regime recognition algorithm dynamically switches to another control recipe to restore the desired HRH mode.

Future Directions

Methods for ensuring personnel safety have been largely systematized in existing tokamak devices. Anticipated dangers in next-generation devices include the use of larger amounts of radioactive tritium, greater neutron production within the device, and the resulting neutron-activated, plasma-facing materials. These dangers can be mitigated by the experience gained over many decades in the nuclear power industry. In addition, accidents involving the loss of cryogenic coolant for superconducting coils might present a danger to personnel as well as to the device.

New methods are sought to deal with these and other types of off-normal events. Many of the present methods of fault detection and diagnosis execute primarily offline and between plasma pulses. These methods need to be converted to online detection algorithms when steady-state devices are put into use. Currently, much of the knowledge required for detecting faulty tokamak systems resides only in the minds of experienced operators. Also, most present-day tokamaks do not maintain models of support systems able to predict system outputs from measurable signals, which are necessary for model-based fault detection. Operator knowledge must be captured, and models of tokamak support systems must be developed so that the knowledge and models may be incorporated into online fault diagnosis software.

For faults that can lead to device safety issues, present methods for controlled shutdown of the plasma pulse must be further developed and expanded to include a greater number of faults. In particular, reliable and safe online methods for remediation of large energy events must be implemented and proven. For example, mitigation of plasma disruptions through massive gas puffing is now being implemented and tested on several experimental devices. The next step is to make these methods part of the routine operation of a device.

EDGE LOCALIZED MODES

A defining feature of high energy confinement (H-mode; see "Tutorial 19") tokamak plasmas is a region of reduced thermal and particle diffusion near the plasma boundary, called the edge transport barrier (ETB) ("Tutorial 20"). Although the high performance of H-mode plasmas results from high pedestal temperatures and densities (Figure 5) obtainable with an ETB, the very low transport in the edge region generally leads to a rise in the gradient of the pressure distribution near the edge, which triggers an instability localized to the plasma edge known as the edge localized mode or ELM [30].

By using photodiodes, ELMs are most often observed as bursts of light from excited hydrogen or deuterium atoms [Figure 6(a)] in regions where the ELM power flux reaches the vessel wall. The magnetohydrodynamic instability that is believed to be responsible for the larger ELMs in Figure 6(c) also perturbs the magnetic field. This perturbation can be observed on magnetic probes mounted on the vessel wall [Figure 7(b)].

The physics processes of the ELM are not completely understood, although significant progress is being made. Theories based on ideal MHD ("Tutorial 3" in [2]) appear to be in good agreement with the early linear phases of mode growth. The later nonlinear growth of the mode is an active area of research. Figure 8 shows the mode structure in the nonlinear growth phase as predicted by the model of [33]. This figure is

consistent with the intuitive picture of ELMs, namely, that the nested flux surfaces characterizing ideal MHD are broken by the instability and, consequently, particles and heat can be removed through the plasma edge.

The three ELM types that are observed in most tokamaks [30] are summarized in Table 1. The different types are experimentally distinguished by the dependence of the ELM frequency on heating power df_{ELM}/dP (Figure 6), the density of the plasma, and the shaping applied to the plasma cross section.

Each ELM causes a collapse of the ETB and can cause a loss on the order of 5% of total plasma stored energy on a very short timescale. The ETB forms again following the ELM and the energy confinement of H-mode discharges with ELMs remains superior to discharges with no ETB. However, the large power loss during the ELM, projected to be tens of gigawatts in a power-producing reactor, creates severe difficulties in the design of the tokamak power exhaust handling structures (Figure 9). Work on ELMs has focused on developing techniques for 1) reducing the ELM power loss, either by reducing the total ELM energy loss or by extending the time during which the energy is lost, or 2) enhancing the particle transport in the ETB or raising the ELM instability threshold to keep the pressure gradient below the critical level that triggers the ELM. Both of these approaches must also maintain a high-quality ETB for good overall confinement.

An ELM control technique that uses the second approach is to operate the tokamak with "ELM-free" discharges, which have previously been observed in tokamak experiments. In these discharges, the plasma has a high critical (threshold) pressure gradient for the ELM instability, and input power is kept sufficiently low so that this critical pressure gradient is not reached. However, this technique results in another difficulty. Impurities are continuously produced by plasma interaction with device components that face the plasma or as products of fusion reactions. Impurities entering the plasma edge are generally ionized in or near the ETB and are then transported inward to the plasma core, where they interfere with fusion power production. ELMs reduce the source of these impurities by removing them periodically in their region of ionization. Thus, ELM-free discharges often exhibit impurity accumulation and are not considered to be viable solutions. Therefore, any technique that eliminates the ELMs must also provide an alternative mechanism for reducing the impurities in the plasma. Furthermore, ELMs provide a mechanism for density control by moving particles from the plasma interior to the scrape-off layer, where the particles can be pumped out of the vessel ("Tutorial 6" in [7]). If ELMs are eliminated, an alternative method for density control is needed.

Experimental Approaches to Control

Although several promising approaches for reducing or eliminating ELMs have been explored, none present a clear solution path. An ideal method is one that provides transport of particles out of the plasma, but without the associated heat transport,

Tutorial 20: Edge Transport Barriers

Explanation of the ELM instability centers on the transport and MHD behavior in the edge transport barrier of the plasma (Figure A). In contrast to global modes such as the RWM (see the RWM section of this article), the ELM is primarily localized to this edge region. The height of the temperature pedestal (Figure A) acts roughly as a multiplier for temperatures inside the plasma. The greater the pedestal height, the greater the total energy content of the plasma. Inside the knee, the temperature is approximately ten times that of the sun's center (1,000 eV), while exterior to the plasma it is about 10 eV. The source of the ELM instability is the resulting large pressure gradient in the edge region. During an instability, up to 25% of the pedestal energy can leave the plasma and be deposited on plasma-facing components.

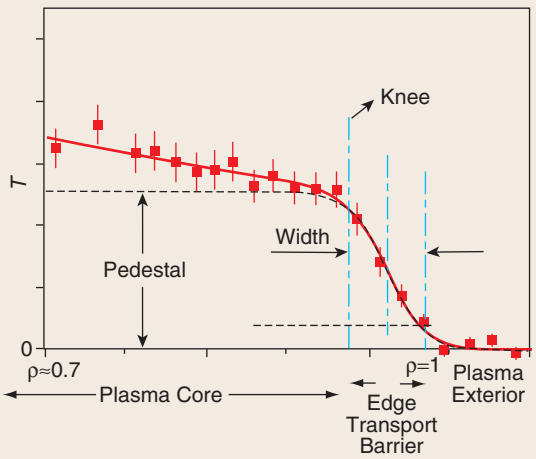

FIGURE A Definitions relevant to ELMs. The solid red curve is fit to the measured electron temperature data. Lines through the data points indicate plus or minus one standard deviation (estimated) from measurements. The edge transport barrier (ETB) is a region at the edge of the plasma that is a barrier to the transport, or diffusion, of heat and particles out of the plasma. The ETB and other forms of transport barrier are characteristic of high energy confinement mode (H-mode) plasmas, since they tend to prevent heat from escaping the plasma. Width of the ETB is defined to be the width of the steep gradient region in the electron temperature profile. This edge region is defined to be the region between the knee of the fitting function and the plasma last closed flux surface. The pedestal in temperature coincides with the plasma interior region. (The terminology in the literature is inconsistent, since "pedestal" is sometimes used to refer to the edge region.) Since the pressure profile in H-mode plasmas takes a similar form, in discussions of edge transport barriers, temperature and pressure are often used interchangeably. However, pressure can sometimes have a narrower steep gradient region. The close proximity of the high-pressure region inside the ETB and the low-pressure region outside the ETB is the source of the ELM instability.

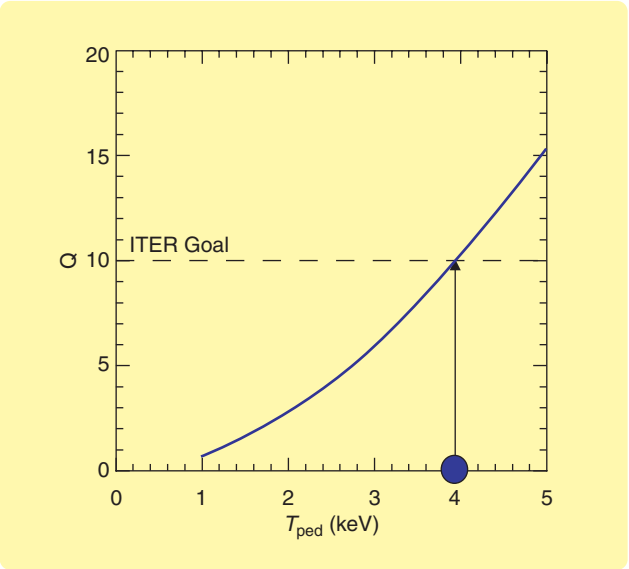

FIGURE 5 Projected dependence of Q on pedestal temperature. The ratio Q of fusion output power to additional heating power into the plasma is a measure of efficiency of fusion power production. This plot assumes a fixed 40 MW of available input power and constant density across the pedestal (Figure A). The pedestal temperature must be maintained at approximately 4 keV to sustain the ITER target value of Q = 10.

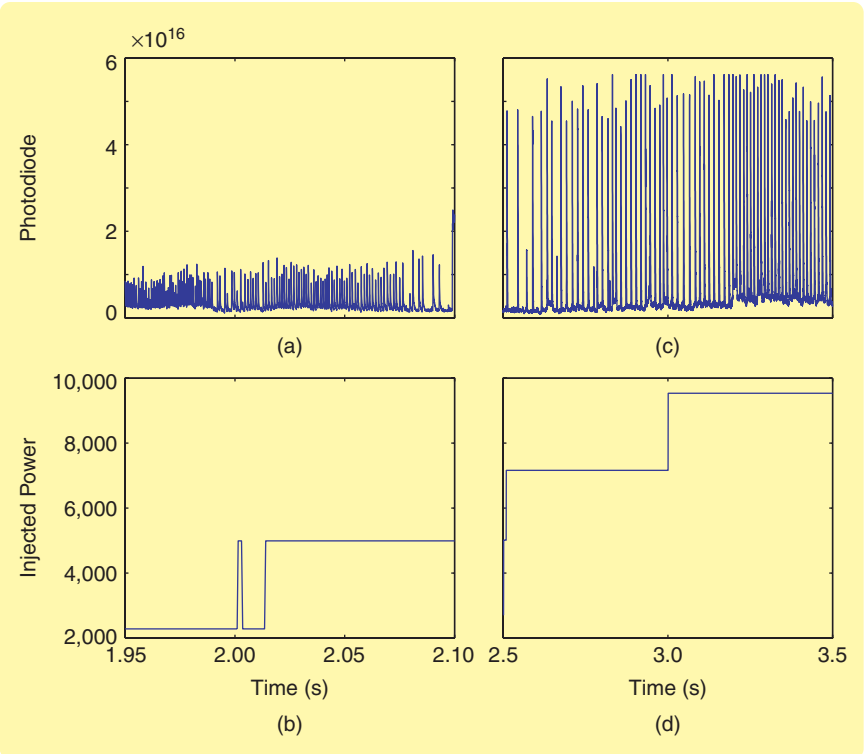

FIGURE 6 Dependence of different ELM types on injected power: (a) shows detected light emission for Type III ELMs, and (b) shows neutral beam power injected into the plasma during the same time; (c) shows detected light emission for Type I ELMs, and (d) shows simultaneous neutral beam power injected into the plasma. One characteristic that distinguishes Type I and Type III ELMs is their response to increases in injected power. The frequency of Type I ELMs increases with increasing power while the frequency of Type III decreases. Another characteristic is the typically much larger peak amplitude of Type I ELM light emissions.

which degrades energy confinement. None of the current methods are sufficiently advanced to attempt feedback control.

Several experiments have shown that regular injection of deuterium fuel or impurities in the form of frozen gas pellets or by gas puffing can trigger or modify ELMs. For example, experiments at the ASDEX-U tokamak [34] show that repetitive deuterium pellet injection can trigger more frequent, smaller ELMs. Energy losses are thus spread over longer times, with smaller peak losses. The resulting loss of confinement is not as severe as with naturally occurring ELMs. Using this method, only ELMs initiated by pellets occur. Gas fueling has also been shown to produce ELMs of smaller size. In cases where the Type I ELM size is reduced by increased gas fueling, the reduced ELM size is believed to be caused by a narrowing of the steep pressure gradient region near the separatrix relative to the ETB width (see "Tutorial 20"). The narrower pressure gradient region enables instabilities to be triggered more easily, allowing less time for energy to build up between ELMs. In present experiments, this effect also results in reduced core stored energy. However, in a reactor-scale tokamak, it is speculated that a confluence of factors enabled by the expected higher pedestal temperature can mitigate this reduction in performance.

One class of experiments shows that Type I ELMs can be converted to Type II or III by oscillation of the plasma position. At TCV [35], vertical position oscillations of a few millimeters induced higher-frequency ELMs, some apparently locking to the oscillation frequency. If this oscillation is done on a frequency greater than the natural ELM frequency, the ELM size is reduced. The cause of the ELM triggering is unclear, although there is speculation that the vertical motion induces current in the plasma edge triggering the instability. It is unknown whether this technique will be compatible with good performance in a reactor-scale tokamak.

Experimentalists at the Alcator C-Mod tokamak have discovered an ELM-free H-mode regime called enhanced D-alpha (EDA) [36]. This mode exhibits enhanced particle transport without an accompanying increased energy transport. This regime is characterized by the presence of high-frequency (>100 kHz) plasma edge fluctuations that seem to provide the necessary mechanism for enhanced particle transport for density control and for removing impurities. Although the EDA has the desired characteristics, other devices have so far been unable to reproduce this

mode, except, perhaps, for the JFT-2M tokamak [37]. In addition, the continuous edge instability is thought to be associated with high edge resistivity ("Tutorial 9" in [7]) and thus might not occur in a reactor-scale tokamak.

Experiments at DIII-D have demonstrated a regime called quiescent H-mode (QH-mode) [38], which allows ELM-free operation. A key feature of the regime is an edge electromagnetic oscillation, also known as the edge harmonic oscillation (EHO) [39]. The EHO enhances the particle transport through the edge without significantly increasing the thermal transport. The QH-mode operation has also been demonstrated at ASDEX-U [40], and QH-mode periods have been seen in discharges in JET and JT60-U. Although QH-mode operation occurs in a more reactor-relevant regime than EDA, this mode appears to require toroidal rotation of the edge plasma opposite to the direction of the plasma current.

A method for controlling large ELMs in high-confinement plasmas by creating a stochastic magnetic boundary is demonstrated in [41]. A stochastic boundary refers to a randomization of magnetic flux contours at the plasma edge in place of the nested contours characteristic of ideal MHD. Experiments at DIII-D and subsequent analysis show that imposition of a nonaxisymmetric field can randomize the flux at the plasma edge and provide a means for steady-state transport of particles out of the plasma, in contrast to the impulsive transport of ELMs. ELMs are reduced or eliminated while maintaining a high H-mode pedestal ("Tutorial 20"). Initial experimental results were obtained in plasmas with high collisionality at the plasma edge and used low magnetic perturbation amplitudes. Collisionality refers to the frequency with which particle collisions occur. More recently in [42], in experiments with low edge collisionality, conditions similar to those expected in ITER, the use of high magnetic field perturbations completely eliminated ELMs, similar to the QH-mode regime. Present stochastic boundary experiments use steady-state nonaxisymmetric magnetic perturbations, which have the side effect of slowing plasma rotation and can result in destabilizing the RWM instability. (See the "Stabilization of the RWM" section.) A modification of the method that uses an oscillating field perturbation may not have this problem. The stochastic boundary approach is promising for ITER because it is practical to implement, although some aspects of the physics remain unclear.

Future Directions

An H-mode regime with Type I ELMs has been chosen as the standard operating scenario ("Tutorial 13" in [10]) for ITER [43] because it is capable of being sustained in steady state with high confinement. Ongoing investigations of ELMs have focused on evaluating the adequacy of this choice as well as considering possible alternatives. These alternatives so far consist of both modified operating regimes that avoid Type I ELMs and open-loop methods to alter the character of the ELM instability. Some of these methods offer the possibility of feedback control for ELM suppression. For example, the mechanism for ELM suppression in the stochastic boundary approach with low edge collisionality plasmas is caused by a

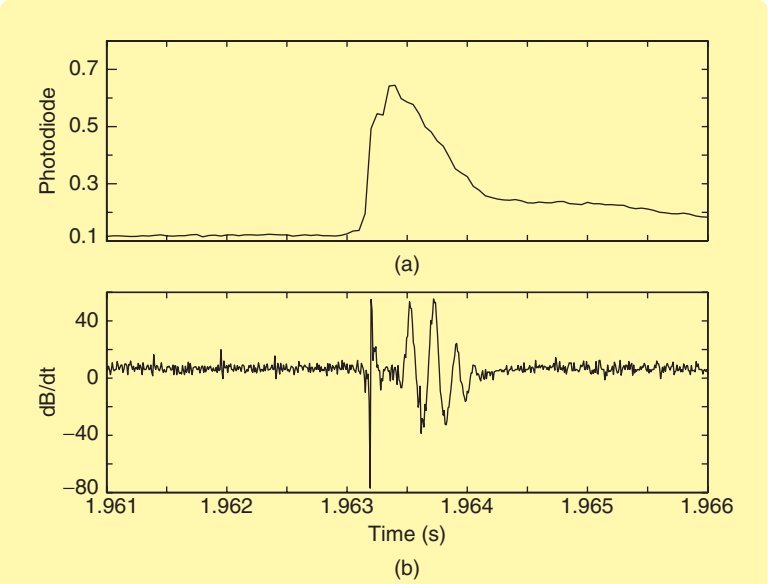

FIGURE 7 The magnetic character of an ELM. The curve in (a) is an expansion of a single instability similar to those shown in Figure 6(c). The curve in (b) is a measurement of the derivative of magnetic field at the outboard midplane showing magnetic behavior simultaneous with the light emission in (a).

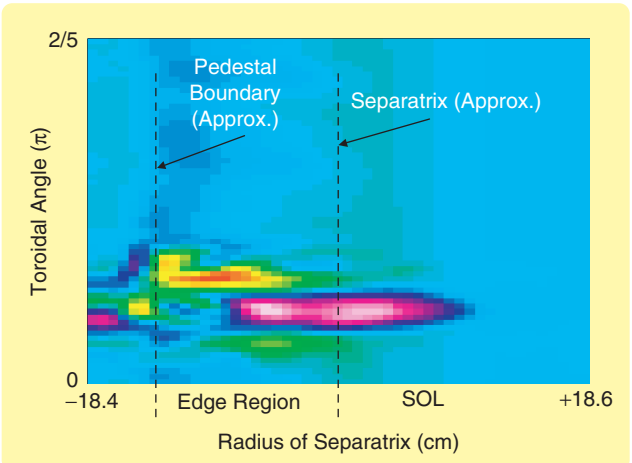

FIGURE 8 Intensity plot of the perturbed density at the plasma outer midplane during the later nonlinear phase of a simulation of the growth of the edge localized mode. The early phase of the mode growth is linear and approximately represented by ideal MHD. The local nature of the mode growth is illustrated with the "finger" of plasma radiating out from the plasma edge toward the vacuum vessel wall. This plasma finger also extends along the magnetic field (into and out of the page). Large transport through the walls of the finger or the breaking off, or magnetic reconnection, of the finger are possible mechanisms for the ELM energy loss.

TABLE 1 Experimental characteristics of the three ELM types. The ELM type with the widest operational range, Type I [Figure 6(c)], allows large pressure in the ETB but the energy loss ΔW_{ELM} at each ELM is also large. The symbol W is used in plasma physics to denote quantities of energy. The pedestal energy W_{PED} is defined as the pressure on the inside edge of the ETB times the plasma volume. Note that pedestal energy is not the same as total stored energy. The Type II ELM has low ELM energy loss and high ETB pressure but is observed only in a limited range of plasma shaping and density that may not be applicable to a tokamak reactor. The Type III ELM [Figure 6(a)] has a wider operational range than the Type II and low ELM energy loss but also reduced energy in the pedestal. The pedestal energy W_{PED} and density shown here are values relative to the conditions under which Type I ELMs occur.

Type	W_{PED}	ΔW_{ELM}	df_{ELM}/dP	Density	Shaping
I	1	0.05–0.25 W_{PED}	> 0	1	Any
II	1	$< 0.01\ W_{PED}$	< 0	$\gg 1$	Strong
III	$< 2/3$	$< 0.01\ W_{PED}$	< 0	$\gg 1$ or $\ll 1$	Any

reduction in the edge pressure gradient ("Tutorial 20"), a potentially measurable quantity. The amount of reduction seems to depend on the magnetic field strength and how well the pitch ("Tutorial 16" in [1]) of the applied magnetic field matches the field at the plasma edge. These control actuators and measurements suggest a possible mechanism for feedback control of ELMs. Similarly, since ELM frequency is apparently controllable by injecting pellets or gas or by oscillating the plasma, it is feasible to think in terms of controlling the ELM frequency in feedback using these actuation methods.

STABILIZATION OF RESISTIVE WALL MODES

In this section, we discuss one of the major tokamak nonaxisymmetric instabilities, namely, the resistive wall mode (RWM). The RWM is a form of plasma kink instability under the influence of a resistive wall. The word kink is appropriate to characterize the RWM behavior, which is similar to a garden hose kinking when it is suddenly pressurized (Figure 10). The entire plasma configuration deforms in a helically symmetric manner. The toroidal mode number n ("Tutorial 4" in [2]) is used to identify the helicity of the deformation. For RWM control, we are primarily interested in the lowest mode number $n = 1$ since the $n = 1$ instability is the first to occur with rising pressure. Although the achievable plasma pressure in power reactors is expected to be limited by the $n = 1$ mode, it is predicted that the $n = 2$ mode will also become unstable if the $n = 1$ mode is stabilized and the pressure continues to rise.

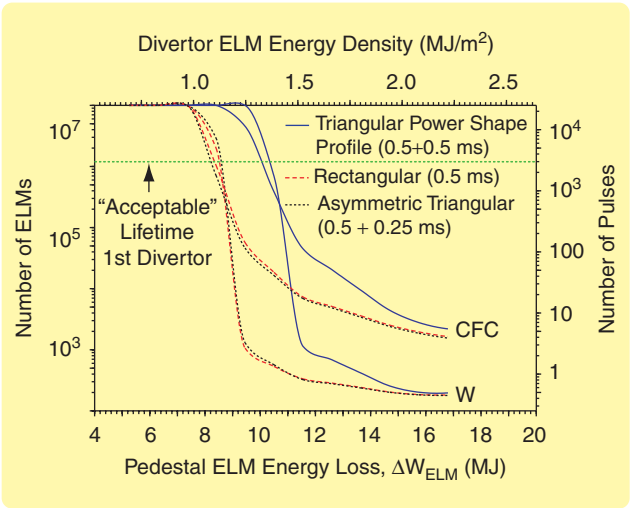

FIGURE 9 Expected erosion lifetime of ITER divertor plasma-facing components (Tutorial 6 in [7]), expressed in terms of the number of ELMs or corresponding ITER full power pulses, as a function of ELM energy loss from the pedestal ΔW_{ELM} (see Table 1). Curves are shown for two materials, carbon fiber composites (CFC) and tungsten (W), and for three different approximations to the power signal during an ELM. The lifetime of the ITER divertor drops quickly as the energy lost per ELM increases. Uncertainties in extrapolating expected ELM energies from present devices make it difficult to know precisely what to expect in the ITER device. (Reproduced from [32] by permission of G. Federici and the Institute of Physics.)

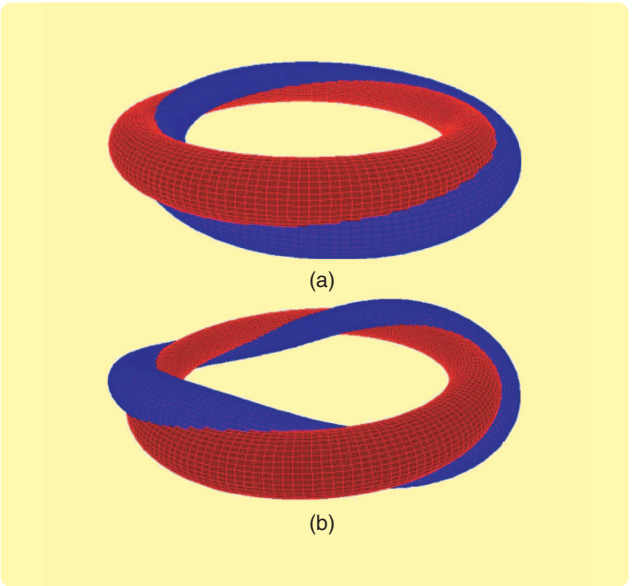

FIGURE 10 Illustration of kink deformations of a circular cross-section plasma, greatly exaggerated for illustration. The red torus represents a circular cross-section plasma before deformation. The blue surface represents the deformed plasma: (a) shows an $n = 1$ kink, and (b) shows an $n = 2$ kink, in which the plasma perturbation repeats itself twice as the toroidal angle varies from 0 to 2π. In each case, the deformation follows a helical path with respect to the undeformed plasma.

When the plasma undergoes a nonaxisymmetric distortion as in Figure 10, the current flowing in the plasma moves with it. The magnetic flux and field generated by this current also moves with the fluid distortion. This moving magnetic field induces eddy currents in the surrounding conductive structures similar to the way in which eddy currents are induced by the vertical instability ("Tutorial 14" in [1]). These induced currents, in turn, generate magnetic fields that oppose the plasma deformation, as in the case of the vertical instability. The overall effect of the presence of a conducting wall is to transform a plasma deformation with an extremely fast growth time of a few microseconds into a combined plasma/wall system with an instability having a growth time on the order of the resistive decay time of eddy currents in the surrounding materials, that is, a few milliseconds. This slower growth enables the use of feedback to control the RWM instability.

The magnetic field motion due to the plasma fluid deformation is observable outside the plasma by magnetic sensors. Even though the deformation of the plasma surface cannot be directly measured in real time, the magnitude and direction of the deformation can be inferred from the external magnetic sensor measurements (Figure 11). Magnetic sensors are structurally simple and robust, and thus are viable for magnetic feedback control. Offline diagnostics are used for developing understanding and modeling of the physical processes. Examples of the diagnostic measurements used in RWM analysis are shown in Figure 12.

The Physics of the RWM

According to MHD theory, a sufficiently high plasma pressure makes the RWM unstable when the surrounding wall structure is located far from the plasma surface. The plasma pressure threshold for this instability is expressed in terms of a critical value of normalized beta β_N ("Tutorial 2" in [2]). The unstable eigenmode could, in theory, be stabilized by the mode-induced eddy currents in the wall if the plasma were surrounded by a perfectly conducting wall within a critical distance. A perfect conductor is one without resistance, implying that there is no resistive decay of the stabilizing eddy currents induced by the eigenmode. In actual devices, the wall current decays due to resistive losses, and the mode amplitude grows with a growth time that is a fraction of the wall time constant. The critical value of beta for which the plasma becomes unstable without a perfectly conducting wall is called the no-wall beta limit. With a further increase of plasma pressure, the RWM would become unstable even in the presence of a perfectly conducting wall. The value of beta for which this ideal instability ("Tutorial 17" in [1]) occurs is called the ideal-wall beta limit.

Ideal MHD gives a detailed prediction of the structure of the RWM, as illustrated in Figure 13. MHD also predicts that the RWM amplitude is larger at the outer radius side of the plasma than at the inboard side. This larger amplitude is due to the nature of the confining toroidal field, which decreases away from the torus axis of symmetry (the Z axis in Figure A in "Tutorial 1" in [2]) so that the magnetic field pressure is weaker at the outer radius. This difference in pressure increases the RWM perturbation amplitude at the outer edge of the plasma, which suggests that an actuator located at the outer radius of the plasma is favorable and should be effective for RWM control.

According to ideal MHD, the RWM structure inside the plasma fluid is complex [Figure 13(a)]. However, when considering methods for stabilizing this mode, fluid deformation is not the focus of attention. Instead, these methods focus on the magnetic field perturbation associated with the plasma fluid deformation, since a number of real-time sensors are available to measure this perturbation (Figure 11) and simple models of the RWM can be developed. Experimental studies [45]–[50] reveal characteristics of the RWM and their relation to ideal MHD predictions:

1) The spatial structure of the RWM agrees with the ideal MHD theoretical prediction (Figures 13 and 14). The RWM exhibits a structure that is global, extending from

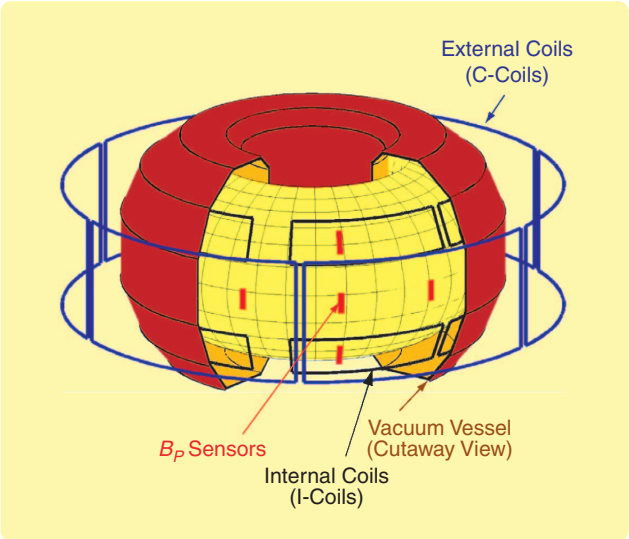

FIGURE 11 RWM real-time control sensors and actuators currently installed on the DIII-D device. The vacuum vessel, represented by the brown surface, is cut away to show internal detail. The plasma is represented by a yellow surface. Typical sensors for radial flux measurement are provided by window-frame-shaped saddle loops (Tutorial 8 in [7]). Saddle loops used for RWM control (not shown) are as large as the external actuator coils, known as C-coils, and located concentrically with those coils; these saddle loops are also referred to as radial flux loops. Radial flux is equal to the integral $\psi = \int_{A_l} B_r dA$ of radially directed magnetic field B_r normal to the wall over a broad area, where A_l is the area subtended by the loop. Although, strictly speaking, these saddle loops measure radial flux, measurements made by these sensors are often referred to as radial field measurements because of this integral relationship between field and flux. The poloidal field B_p sensors, shown in red, are magnetic probes. These sensors are mounted on the vessel wall and measure the local magnetic field component tangent to the wall. For actuation, the C-coil set, shown as blue rectangles, consists of six coils located on the midplane outside the vacuum vessel. The I-coil set, shown as black rectangles inside the vessel, consists of two sets of six coils at upper and lower off-midplane angles, installed between the vacuum vessel wall and the plasma-facing carbon tiles.

the plasma core to outside the vacuum vessel, where we define this mode as the combined magnetic field produced by the displaced plasma fluid and the conducting structures.

2) The existence of a threshold in plasma pressure for the onset of the RWM agrees with ideal MHD theory.
3) When a nonaxisymmetric external magnetic field exists, the mode responds only to the component of the external field that matches the mode's own field structure. The mode amplitude is amplified proportional to the external field, behaving like a magnetic field resonance (discussed below).
4) Beyond the ideal MHD framework is a surprising observation: the mode can be completely stabilized by rotating the plasma if the rotation is above a critical value.
5) The RWM can be stabilized by plasma rotation for well over the ideal MHD timescale ("Tutorial 17" in [1]), while the mode spatial structure remains unchanged even after the wall eddy current disappears. The sustainment of a single mode pattern over a long period is encouraging for developing simple magnetic control techniques. This spatial invariance is described as mode rigidity.
6) However, the finite amplitude of the long-sustained RWM reduces the bulk plasma rotation, leading to a less-stable high-pressure plasma.

These observations provide the rationale for two approaches for stabilizing the RWM. The first approach uses feedback control to oppose the moving field that accompanies the growth of the mode. We refer to this approach as magnetic control. The rate of growth of the mode is slowed sufficiently by the conducting wall to make a feedback process feasible. The existence of a single dominant mode allows for simpler models of the plant to be controlled. An example of the coil arrangement used to excite the nonaxisymmetric field necessary for RWM control is shown in Figure 11.

The second approach for RWM control is the use of plasma rotational stabilization. In present-day tokamaks, neutral beam injection (NBI; see "Tutorial 9" in [7]) supplies an ample amount of angular momentum input for maintaining rotation of the plasma fluid, leading to the stabilization of the RWM mentioned above. However, it is not obvious whether sufficient plasma rotation can be achieved in power-generating fusion reactors. Thus, magnetic feedback control is actively being pursued for use in future devices.

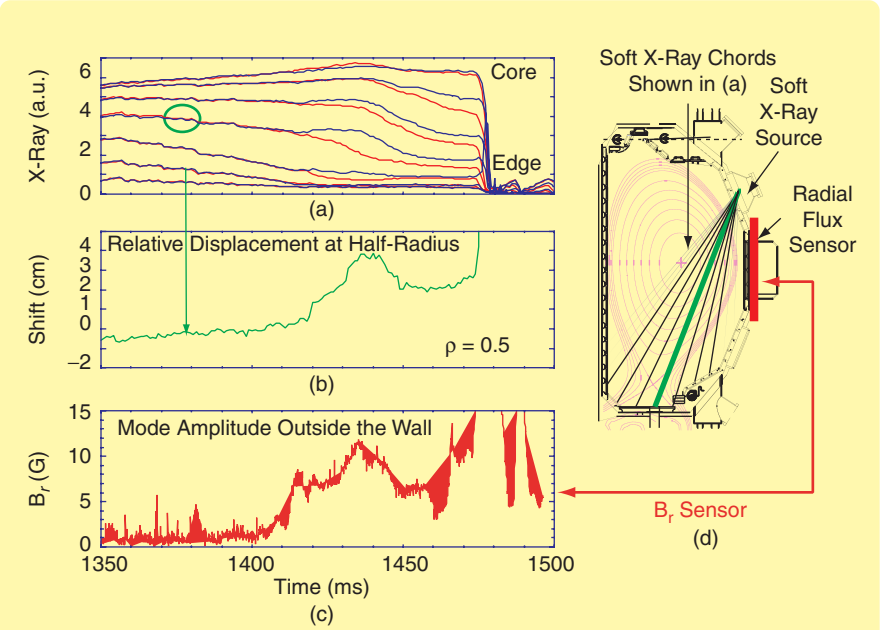

FIGURE 12 Observation of an RWM inside a plasma by the soft X-ray diagnostic and outside the vacuum vessel by a magnetic sensor. Time-dependent measurements of soft X-ray data measured at two toroidal locations, spaced 150° apart, are indicated in (a) by red and blue lines (a.u. = arbitrary units). These measurements can be used to estimate plasma fluid displacement. The curve in (b) shows the displacement of the plasma fluid corresponding to the soft X-ray line circled in (a). The amplitude of the radial magnetic field measured just outside the vessel during this time is shown in (c). Note the strong correlation between the fluid displacement in (b) and magnetic field growth in (c). A DIII-D cross section illustrating the soft X-ray and magnetic field measurement locations is shown in (d). The thick green soft X-ray chord corresponds to the signal shown in (b). The helical $n = 1$ internal mode structure is observable as differences in displacement measured by the two soft X-ray arrays (a). The soft X-ray diagnostic detects the X rays emitted by a residual amount of impurity ions caused by electron bombardment. This diagnostic is not sufficiently robust for real-time use, since the signals are also sensitive to minor changes of other plasma properties.

Models of the RWM Instability

In this section, we describe basic models that are in use for stabilizing the RWM. Initially, we assume there is little or no bulk plasma fluid rotation. Thus, we concentrate on the magnetic aspects of the control problem. Models for magnetic control ignore the internal details of the plasma, focusing instead on the behavior of the magnetic field structure on the plasma surface. A common method for modeling the unstable mode is to replace the spatial perturbation of the plasma with an equivalent perturbation of surface current on a spatially fixed plasma boundary. The spatial and current perturbations are equivalent in the sense that they both produce the same magnetic field perturbation. The surface current distribution can be calculated from the geometrical shift of the plasma surface. The eddy current pattern on the wall can also be calculated once the plasma surface current pattern is determined. The plasma surface current and wall eddy currents are illustrated in Figure 14

through plots of magnetic field normal to the plasma boundary.

Using the assumption of a rigid mode structure mentioned above, the spatial distribution of current on the plasma surface and the wall remain intact while only their magnitudes change. Using the surface current representation of this mode, we can construct a state-space model of the plant with states given by current I_p on the plasma surface and current I_w in surrounding passive (wall) structures. These variables are scalar multipliers of the spatially fixed distributions of current on the plasma surface and in the wall. The external control coil current I_c represents the scalar multiplier of a single spatial distribution of currents produced by multiple coils chosen to best match the distribution of the eigenmode. These variables represent perturbations, due to the appearance of the nonaxisymmetric RWM, from axisymmetric, purely toroidal currents needed to maintain the axisymmetric equilibrium.

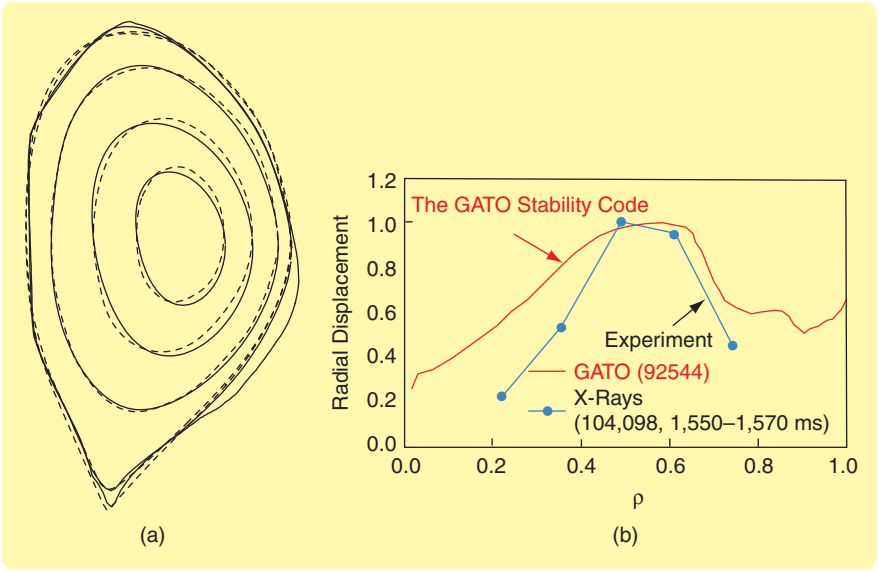

FIGURE 13 Comparison of theoretically predicted RWM structure with measurement. (a) The structure of the RWM displacement from the axisymmetric plasma is computed by the GATO ideal MHD code [44]. The dashed lines represent constant flux surfaces before deformation. Solid lines represent these flux surfaces after deformation by the RWM. Perturbations are greater at larger radii R because of the inverse dependence of the confining field on radius. The displacement magnitude is exaggerated for illustration. (b) A comparison of the experimental plasma fluid radial displacement estimated using soft X-ray data (see Figure 12) and the mode radial displacement predicted by GATO. The magnitude is normalized to the maximum amplitude perturbation (about 8 cm) near $\rho = 0.5$. (The normalized flux coordinate ρ is defined in Tutorial 5 in [1].) The prediction accuracy is adequate for control, at least in the region where data is available for comparison.

We now discuss RWM behavior using a simple cylindrical model [51], [52]. These cylindrical models, in which plasmas are assumed to flow in an infinitely long cylinder, are a first step in developing an understanding of the phenomena that occur in the "bent" cylinder constituting a torus.

The pressure balance on the plasma surface between the internal plasma pressure and the external magnetic field pressure leads to the circuit-like ("Tutorial 11" in [10]) equation

$$L_{\text{eff}}\, I_p \;+\; M_{pw}\, I_w \;+\; M_{pc}\, I_c = 0, \tag{1}$$

where the constants M_{ab} represent mutual inductance between conductors a and b (see Figure 15), the effective self inductance L_{eff} is given by

$$L_{\text{eff}} = \frac{L_{\text{p}} C_\beta}{(C_\beta + \Delta M)}, \tag{2}$$

where

$$\text{C}_\beta = \frac{\beta_{\text{N}} - \beta_{\text{N.no-wall}}}{\beta_{\text{N.ideal-wall}} - \beta_{\text{N.no-wall}}},$$

$\Delta M = L_p L_w / M_{pw}^2 - 1$ is related to the wall stabilization effect, and L_p represents self-inductance of the plasma. The constant C_β is a measure of the stability of the plasma to RWMs. When $C_\beta < 0$, β_N is below the no-wall limit and the RWM is stable. Note that $\beta_{\text{N.ideal-wall}}$ is always greater than $\beta_{\text{N.no-wall}}$. When $C_\beta > 1$, β_{N} is above the ideal-wall limit and the plasma cannot be practically stabilized. Efforts at active stabilization aim at the interval $0 < C_\beta < 1$. The wall eddy current and the active coil current are modeled by circuit equations

$$\begin{aligned} M_{\text{wp}}\dot{I}_{\text{p}} + L_{\text{w}}\dot{I}_{\text{w}} + M_{\text{wc}}\dot{I}_{\text{c}} + R_{\text{w}} I_{\text{w}} &= 0 \\ M_{\text{cp}}\dot{I}_{\text{p}} + M_{\text{cw}}\dot{I}_{\text{w}} + L_{\text{c}}\dot{I}_{\text{c}} + R_{\text{c}} I_{\text{c}} &= V_{\text{c}}. \end{aligned} \tag{3}$$

Here, the constants R_a represent resistance in conductor a and, as in (1), constants M_{ab} and L_a represent mutual inductance and self-inductance, respectively (Figure 15). The ordinary differential and algebraic equations (1) through (3), which constitute the overall circuit model, can be expressed by means of a Laplace transform as

$$(Ms + R)I = V, \tag{4}$$

where s is the Laplace transform variable,

$$M = \begin{bmatrix} L_{\text{eff}} & M_{\text{pw}} & M_{pc} \\ M_{\text{wp}} & L_{\text{w}} & M_{\text{wc}} \\ M_{\text{cp}} & M_{\text{cw}} & L_{\text{c}} \end{bmatrix}, \quad R = \begin{bmatrix} 0 & 0 & 0 \\ 0 & R_{\text{w}} & 0 \\ 0 & 0 & R_{\text{c}} \end{bmatrix},$$

$$I = \begin{bmatrix} I_{\text{p}} \\ I_{\text{w}} \\ I_{\text{c}} \end{bmatrix}, \quad \text{and} \quad V = \begin{bmatrix} 0 \\ 0 \\ V_{\text{c}} \end{bmatrix}.$$

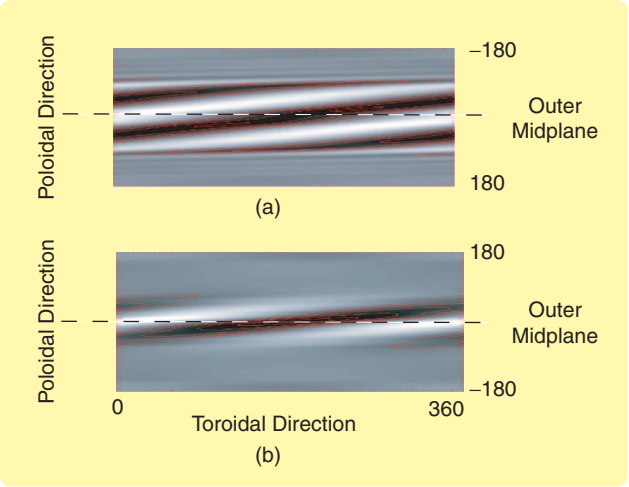

FIGURE 14 Normal magnetic field perturbation on the plasma surface due to an RWM as calculated with the GATO ideal MHD code [44]. Perturbations are relative to the normally axisymmetric, that is, independent of toroidal angle, values that occur in the absence of an RWM. Perturbed normal field at the plasma surface due to the plasma current is shown in (a), while the corresponding perturbed normal field at the plasma due to the wall currents is shown in (b). A poloidal angle of 0° corresponds to the outer midplane (see Figure A. in Tutorial 1 in [1]). The normal fields shown reflect the pattern of current flow in the two conducting surfaces. Lighter colors are more positive, darker more negative. The eddy current on the wall is induced by perturbations of the plasma surface current as discussed in the text. The maximum plasma surface current perturbation occurs at the outer midplane and decreases rapidly toward the inner radius side. Correspondingly, the maximum eddy current on the wall occurs at the outer radius side since the current is inductively coupled to the plasma current. Note that the pattern is periodic with toroidal period one, so that the toroidal mode number $n = 1$, and that the high and low amplitudes in the mode wind their way in a helical pattern around the torus.

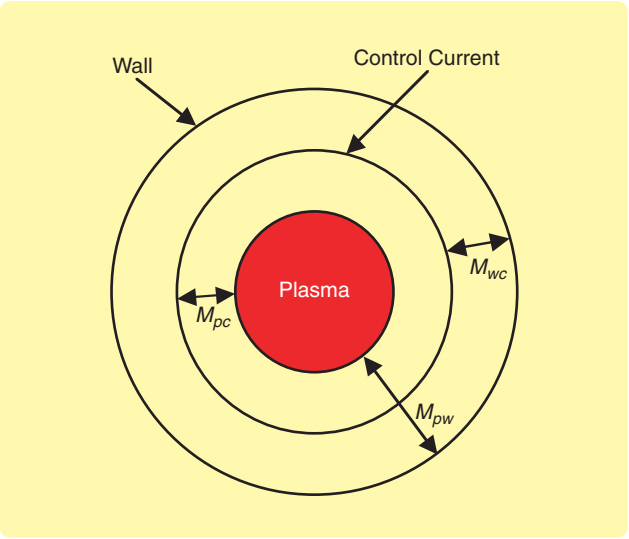

FIGURE 15 Cross section of a cylindrical model of the RWM dynamics. The model shown represents the case where the control coils are inside of the vessel wall. The interaction among current in the plasma, wall, and control coils (subscripts p, w, and c) is determined by the mutual inductance values M. The drawing is not to scale.

Using this formulation, we can treat the RWM control model as if it were a standard circuit equation. The mutual inductances are computed by standard geometric methods [53]. The modified self-inductance L_{eff}, which is the only term that differs from the standard electromagnetic definition (see "Tutorial 11" in [10]), includes the plasma parameters. This approach allows variations in the plasma to be modeled as changes to a single term, namely L_{eff}.

Rotational Stabilization

When the toroidal rotation of the bulk plasma fluid on DIII-D remains above about 6 kHz, the RWM instability is completely stabilized (Figure 16). A primary cause of rotation in experimental devices is the injection of neutral deuterium atoms (intended originally for heating; see "Tutorial 9" in [7]) at an angle nearly tangential to the torus. The momentum of these particles is imparted to the bulk plasma, thereby increasing the rotation. Distinct from the fluid rotation is the rotation of the mode itself, typically at a frequency between 10 and 20 Hz, which is believed to be coupled to the fluid rotation.

To include the effect of plasma rotation in the model of the RWM, we must depart from the previous assumption of a rigid mode at a fixed toroidal angle. The unstable mode maintains the rigid sinusoidal current spatial distribution having a toroidal period equal to one (Figure 14), but now the model does not assume that the mode toroidal angle is constant. The mode may even include a nonzero average rotation speed, with the special case of zero rotation represented in the previous discussion. Thus, the previous representations in which $I_c(t)$, $I_p(t)$, and $I_w(t)$ are scalar multipliers of spatially fixed current distributions are replaced by two-parameter multipliers of the form $I_*(t) = A_*(t)e^{i\phi_*(t)}$, where $\phi_*(t)$ represents the toroidal angle of the sinusoidal distribution with respect to a fixed reference angle and $A_*(t)$ represents the peak amplitude of that current distribution. Now the currents I_c, I_p, and I_w, as well as perturbed magnetic fields B_w due to the wall current and B_p due to the plasma surface current, are represented by complex numbers whose real and imaginary parts represent sinusoidal functions of toroidal angle with peak amplitude in the 0° and 90° toroidal directions, respectively. In this notation, multiplication by $i = \sqrt{-1}$ represents rotation toroidally by 90°.

In general, the mechanisms for combined rotation and magnetic effects on the RWM are not well understood. Using an argument based on the exchange of energy between the plasma mode and external conductors, the model

$$(\delta W_{Iw} + i\Omega_\phi D)B_p = C_{pw}B_w \tag{5}$$

is used in [54] to represent the coupling between changes in the field B_p at the plasma surface and changes in the field B_w at the vessel wall when the plasma is rotating. Although this model is qualitative and somewhat speculative, it is described here to provide insight into the possible mechanisms for experimentally observed rotational stabilization. Here, Ω_ϕ represents the plasma fluid toroidal rotation

frequency and $C_{pw} = M_{pw}^{-1}$ is the inverse of the mutual inductance between the wall and the plasma surface. The quantity δW_{Iw} represents the coupling of RWM energy transferred through the field B_p produced by the plasma to the component of the field B_w that is toroidally in phase with B_p, while $\Omega_\phi D$ represents the energy coupled to the component B_w of that is 90° toroidally advanced. The quantity D represents an unknown dissipation mechanism. This representation is motivated by the following:

1) Experiments show that, when the plasma is rotating, the RWM responds at a different toroidal angle from the angle at which an external field is driven. For example, when the plasma is at steady state with a stable RWM ($\beta_N < \beta_{N.no\text{-}wall}$), if a constant sinusoidal $n = 1$ current $I_c(t) = A_c e^{i\phi_c}$ is applied, so that eddy currents are not excited in the wall, the plasma surface mode responds not at the angle $\phi_p = \phi_c$ but at an angle $\phi_p = \phi_c + \delta\phi$ with $\delta\phi > 0$ [48].
2) A theoretical consideration is that momentum can be exchanged between the toroidally rotating plasma fluid and the RWM, transferring some of the unstable mode's energy to a different toroidal angle.

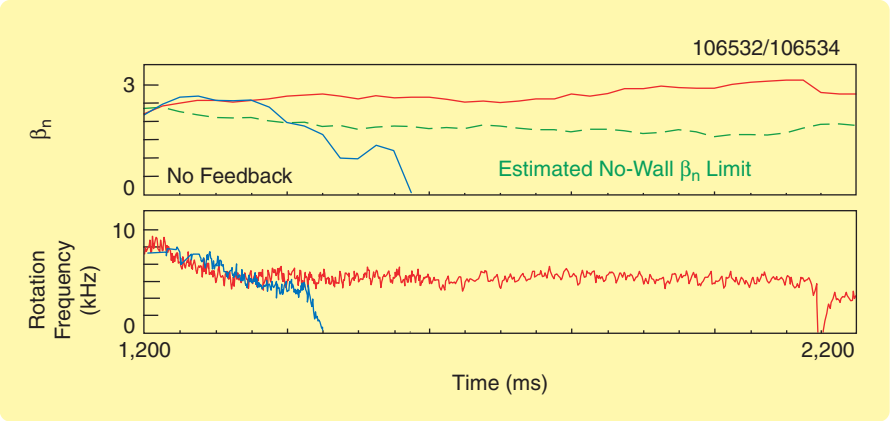

FIGURE 16 Demonstration of suppression of the RWM instability through plasma rotation. As long as plasma rotation remains above a critical frequency [red curve in (b)] of about 6 kHz, the mode remains stabilized, even for plasma beta well above the no-wall limit [red curve in (a)]. When plasma rotation falls below the critical value [blue curve in (b)], the mode becomes unstable, causing loss of plasma pressure [blue curve in (a)], accelerated slowing of the rotation, and, shortly thereafter, loss of the plasma to the unstable mode.

Although there are several candidate models for the dissipation mechanism D, none have been satisfactorily verified experimentally. We present a simplistic explanation of one candidate model that is consistent with the three experimentally observed phenomena: 1) the increase in RWM growth rate as the plasma fluid rotation slows to a critical rotation value, 2) the observed slower rotation of the RWM in the same direction as the rotation of the bulk plasma fluid, and 3) the response described above of a stable RWM to an applied $n = 1$ perturbation that appears at a toroidally shifted location. This model postulates a coupling between the unstable mode and the bulk plasma fluid through a form of viscous friction, as follows. Current is defined as the rate of flow of charged particles. In a current-carrying plasma, an RWM fluid deformation (Figure 10) can be thought of as a change in the pattern of flow of the charged particles that comprises the current in the plasma. This change in flow is seen outside the plasma as a change of flux or field at magnetic sensors. This flow of particles is driven by the sharp difference in total plasma plus magnetic pressures inside and outside of the plasma—the driving force of the RWM instability—and a significant portion of this flow is radially directed (Figure 17). The motion of particles in the plasma can also be influenced by the injection of momentum, for example, from neutral beams. The toroidal particle flow induced by toroidal momentum injection interacts with the particle flows caused by the RWM and vice versa through collisions. To sustain the RWM in a given direction, work is required by the RWM instability to move particles against this toroidal particle flow. This resistance to the motion of particles is essentially the mechanism of viscous friction. The RWM's loss of energy through this work is the conjectured damping mechanism. Assuming this damping mechanism, (5) can be included in (4) by replacing L_{eff} with [49]

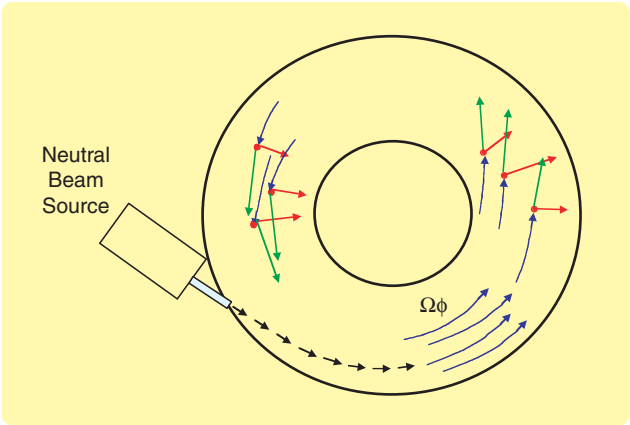

FIGURE 17 A model of the effect of toroidal rotation on the RWM. In a toroidally rotating plasma, individual particles flow with an average speed defined by the bulk fluid rotation frequency Ω_ϕ. An $n = 1$ RWM causes the plasma fluid to bulge radially outward on one side of the torus and inward at a location 180° opposite (see Figure 10). Individual particles driven by the RWM and the component of their velocity vectors induced by the RWM are indicated in red. Continually flowing particles with toroidal momentum (blue arrows) frequently collide with the RWM-driven particles and impart some of their momentum. The resulting velocity (green arrows) of the originally radially directed particles have significant toroidal components.

$$L_{\text{eff}} = \frac{L_{\text{p}}[C_\beta + \alpha_\phi(s + i\Omega_\phi)]}{[C_\beta + \alpha_\phi(s + i\Omega_\phi) + \Delta M]}, \tag{6}$$

where α_ϕ represents the viscous drag coefficient.

The Role of Error Fields

Rotation of the bulk plasma is influenced significantly by the magnetic error field present in the device. The error field is defined as the difference between the slightly nonaxisymmetric magnetic field produced by coils in an as-constructed device and the ideal axisymmetric field that would be produced by an ideally constructed device. The component of the error field resonant with the RWM is that portion of the error field that matches the field pattern of the unstable eigenmode on the plasma surface.

This resonant error field can be represented as an external current source I_{e} acting in a manner similar to the external control coil current I_{c}. The impact of this field can thus be described by replacing I_{c} with I_{e} in the plasma response (1). A changing current, either I_{p} or I_{e}, is required to induce nonzero eddy currents I_{w}. Since the error field is steady state, the perturbed quantity $I_{\text{w}} = 0$ if the RWM is stable. In this case, the plasma response I_{p} to the error field is also steady state, given by (1) as

$$I_{\text{p}} = -\left(M_{\text{pe}}/L_{\text{eff}}\right) I_{\text{e}}. \tag{7}$$

Since M_{pe} is real, the toroidal phase shift $\delta\phi$ is given by (7) as $\delta\phi = \tan^{-1}[-\text{Im}(L_{\text{eff}})/\text{Re}(L_{\text{eff}})]$. The magnitude of the plasma response reaches a large value around the no-wall limit where $L_{\text{eff}} \approx 0$, similar to a resonance effect. This phenomenon is known as resonant (error) field amplification (RFA). As the growth rate of a stable RWM approaches zero from below, the value of L_{eff} also approaches zero. Thus, RFA increases as a stable RWM becomes less stable.

The nonaxisymmetric error field and the resulting amplification of the stable RWM are believed responsible for the rotation slowing observed in Figure 16 through a form of magnetic braking of the plasma rotation. As with rotational damping, there is more than one possible mechanism for the observed rotational slowing. One explanation uses an analogy with the induction motor, which consists of a conductive rotor (the inside part that turns) surrounded by a stator (the stationary outside part that causes it to turn). A magnetic field that rotates around the rotor is set up by properly phased currents flowing in a set of coil windings in the stator. As long as the moving magnetic field rotates faster than the rotor, the field acts on the conductive rotor to generate currents on the rotor surface. A torque is produced on the rotor through the interaction of the induced current with the rotating field (the "I cross B" force; see "Tutorial 14" in [1]). When the magnetic field produced by the stator becomes stationary or reverses direction while the rotor is rotating, the applied torque reverses direction and causes the rotor to slow down. This behavior is directly analogous to a rotating conductive plasma interacting with a stationary nonaxisymmetric magnetic field such as an error field. Slowing of the plasma by the tokamak's intrinsic error field and RFA causes a stable RWM to become less stable, which then increases the effect of the magnetic braking, further slowing the plasma. This process continues until, eventually, the RWM becomes unstable, as shown in Figure 16.

To the sophisticated reader, it is clear that both the rotational damping and the induction motor analogy describe forces that are exerted in both directions. For example, the viscous damping mechanism discussed in the previous section that stabilizes the RWM also results in forces that slow the plasma rotation. Although several damping/slowing mechanisms have been suggested, present experimental data is not sufficient to confirm or refute these mechanisms.

Magnetic Control Approaches

Experimental approaches for magnetic control include correction for external error fields to reduce the magnetic braking on rotation and, separately, magnetic feedback stabilization of the RWM in the absence of plasma rotation. Although the magnetic feedback models allow for mode rotation, they generally do not account for fluid rotation effects. The situation of magnetic feedback with nonzero plasma fluid rotation is not yet sufficiently understood to develop a complete control approach. An experimental RWM controller consists of the observation sensors, sensor logic, digital controller, power supplies, and actuator coils.

Actuators consist of actively driven current-carrying coils, with a picture frame geometry, as seen in Figure 11. The rigidity of the mode simplifies the discussion of the required feedback field. When a nonaxisymmetric field is applied, the plasma perturbation responds only to the component of the field that matches its own mode structure. This response implies that the external coils (C-coils), which primarily produce radial field, are not very efficient since at least half of the magnetic energy does not couple with, and therefore does not affect, the helically shaped mode. The connection flexibility of the internal coil (I-coil) set can be used to provide a field pattern (Figure 14) that more closely matches that of the RWM. The I-coils have the additional advantage of being closer to the plasma, while the appearance of C-coil flux at the plasma is delayed due to shielding by eddy currents in the vessel. For these reasons, the internal coil set is superior to the external coils for feedback control.

Although error fields are determined by the limited accuracy of device construction and are independent of the plasma, the required compensation for these fields depends on properties of the plasma because of the RFA effect. The necessary spatial distribution of the applied corrective field is related to the MHD mode structure, and the required magnitude of the correction depends on the value of L_{eff} according to (7). The magnitude and toroidal angle of the required compensation can evolve slowly in time during the discharge because of changes in plasma properties. In addition, the error field has a complicated nonaxisymmetric distribution that cannot be completely canceled by a finite number of actuator coils. Thus,

compensation cannot be accomplished open loop based on a priori calculations, motivating the use of dynamic error-field correction, which adjusts the error-field correction based on the plasma mode response. This approach leads to a feedback process that executes on a timescale much slower than the wall time. Magnetic control aimed at stabilizing the RWM by directly suppressing the magnetic field that the mode produces requires feedback with a faster time constant equal to a fraction of the wall time. Thus, requirements on actuating coils and power supplies are very different for error-field correction and for magnetic feedback stabilization.

Power systems for tokamak control problems are a challenge due to simultaneous requirements for high voltages and currents and speed of response. RWM control requires a high current of a few kiloamps at near steady state to compensate for error fields and, simultaneously, a fast lower current response to provide magnetic feedback stabilization. Since the conductive wall slows the mode growth to about the time constant of the wall, the maximum bandwidth required for the supply is defined by the inverse of the wall time constant. For example, the DIII-D power supply is designed to have a 3-dB bandwidth of 500 Hz to stabilize plasmas with values of β up to half way between the no-wall and the ideal-wall limits, that is, for $C_\beta = 0.5$ in (2).

Several methods have been investigated to detect mode growth and determine the toroidal angle for feedback. All of these methods are based on the experimental observations that 1) the RWM is well defined by an $n = 1$ distribution and 2) the mode structure is sufficiently rigid to justify representing the mode by an amplitude perturbation that varies sinusoidally in the toroidal direction. The mode can thus be modeled using two parameters representing the amplitude and toroidal angle of the mode or, equivalently, the sine and cosine components $A_{\cos}(t) = A(t)\cos[\phi_0(t)]$ and $A_{\sin}(t) = A(t)\sin[\phi_0(t)]$, where ϕ_0 is the time-varying unknown toroidal angle of the mode amplitude maximum. Most methods investigated to identify the two parameters consist of matrix multiplications $[A_{\cos}(t) \quad A_{\sin}(t)]^T = Gx(t)$, where x is a vector of sensor measurements and G is a constant gain matrix. One approach is to use radial flux sensor measurements $x(t) = [\psi_1(t) \quad \psi_2(t) \quad \psi_3(t)]^T$ at the same radius and at different toroidal angles. Each flux measurement $\psi_j(t)$ represents the difference in magnetic flux measured at two sensors located at the same radius but 180° apart toroidally at the midplane of the torus. This difference reinforces radial flux measurements due to an $n = 1$ mode perturbation while de-emphasizing flux contributions from disturbance sources, such as plasma perturbations having toroidal mode structure with even n. This scheme is called smart shell because the feedback process attempts to minimize the total flux perturbation at the observation point so as to emulate a perfectly conducting wall; eddy currents in a perfectly conducting wall would generate a flux that completely cancels such perturbations.

Another approach to mode detection is to use only poloidal field sensors $x(t) = [B_1(t) \quad B_2(t) \cdots B_m(t)]^T$, where $B_j(t)$ represents the difference in the magnetic field measured at two sensors located at same radius but 180° apart toroidally at the midplane of the torus (Figure 11). This difference is also used to reinforce poloidal field measurements due to an $n = 1$ mode perturbation and to remove magnetic field contributed by axisymmetric variations in the plasma, such as in the plasma shape. This approach is called mode control because the poloidal field sensor measures almost no field directly from the actuator coils, which produce primarily radial field, and thus is more sensitive to the field variations due only to the plasma mode.

A third approach is to determine the mode amplitude and phase using all available flux and poloidal field sensors $x(t) = [\psi_1(t)\,\psi_2(t)\cdots\psi_{n_\psi}(t)\,B_1(t)\,B_2(t)\cdots B_{n_B}(t)]^T$ rather than symmetrically located pairs of either type. Here, the fluxes $\psi_j(t)$ and fields $B_j(t)$ are individual sensor measurements. This method is referred to as the matched filter approach [55] because each row of G defines a spatial matched filter. The first row is matched to the normalized response expected in the set of sensors from a mode with phase $\phi_0 = 0$, while the second row is matched to the normalized expected response from a mode with phase $\phi_0 = 90°$.

The use of a matched filter is motivated by experimentally observed difficulties in rejecting noise and disturbance signals. Rejection of measurement noise can be enhanced by the effective averaging obtained using multiple sensors in a matched filter. The most severe disturbance is due to magnetic sensor responses to ELMs. An ELM is a local mode whose spatial magnetic field distribution is significantly different from the distribution defined by the global RWM, making it a good candidate for rejection using a matched filter. Although use of the matched filter in simulations has been shown to improve the accuracy of the mode estimation, it does not provide a complete solution to rejecting ELM disturbances. The primary difficulty is that, on short timescales, the growth of an ELM disturbance signal includes a large $n = 1$ component similar to the unstable $n = 1$ RWM. The ELM excitation mechanism and mode structure are significantly different, however. These differences motivated the development of a Kalman filter to exploit information contained in the RWM dynamics model to filter out the ELM signals. Simulations [56] and initial experiments indicate that combining the spatial matched filter and dynamic Kalman filter significantly improves the signal-to-noise ratio and rejects ELM disturbances. The use of the matched filter and the Kalman filter require detailed knowledge of the mode spatial distribution. In addition, a Kalman filter requires a good model of the time evolution dynamics of the mode and its interaction with the surrounding structure. The mode dynamics depend strongly on the fluid rotation frequency, however, and this dependence has not been well characterized. Thus, experimental success of this approach relies on the success of ongoing efforts to develop models that combine MHD and rotation effects.

Experimental controllers have been limited to the use of proportional, integral, and derivative (PID) algorithms. Control analyses and simulations using both PID and more advanced control algorithms have also been conducted [57]. Experimental use of the more sophisticated control algorithms has been

limited because of the ambiguity in models due to incomplete understanding of dependence of the RWM on rotation.

Experimental Progress in Stabilizing the RWM

The most important progress in RWM stabilization is the sustainment by rotation of a discharge with $C_\beta \approx 1$ using open-loop, preprogrammed, nonaxisymmetric coil currents to minimize error fields [50]. The reference signal for this current is determined from a heavily time-averaged coil current signal obtained in a nearly identical plasma discharge that uses dynamic error-field correction to define the coil currents. With feedback off and nonaxisymmetric currents programmed in this way, the discharge behavior closely follows the evolution of the discharge with feedback on; the achieved values of β_N and plasma rotation frequency are nearly identical. This open-loop experiment separates stabilization effects due to error-field correction from those due to direct magnetic feedback. The experimental results provide evidence that the resonant component of the nonaxisymmetric field contributes significantly to mode amplification and, consequently, reduces the rotation velocity. Once the compensation is made through the error-field correction, the RFA amplitude does not grow and the plasma does not slow down. The resulting plasma rotation is sufficient to suppress the onset of RWM up to the ideal-wall β_N limit.

Although several experiments [47] show an extension of discharge duration when using magnetic feedback, none have demonstrated long-term stabilization. Analysis [58] and experiments [59] are consistent in showing the superiority of mode control over smart shell control. Motivated by analyses of coil/sensor effectiveness [60], [61], the DIII-D device is equipped with actuators located both inside and outside the vacuum vessel. Use of the internal coils has significantly improved magnetic feedback performance over that achievable with external coils alone (Figure 11).

Future Directions

Experimental and theoretical research continues on the RWM control problem. Many issues are close to being resolved, including the most effective type, location, and configuration of actuators and sensors for magnetic feedback control. Although the data is not yet sufficient for a complete model, much has been learned about the dynamics of the RWM and its interaction with error fields and plasma fluid rotation. Some of the more practical issues such as required current levels, power supply response times, and communication delays that are required for magnetic feedback systems are being addressed.

Significant effort remains to complete RWM model development. Sufficient experimental data needed to either confirm or refute the many candidate magnetic feedback models have been difficult to obtain because of the interaction between error fields, fluid rotation, mode growth, and magnetic feedback. Once models are completely developed and validated, control algorithms that can handle the wide range of RWM conditions can be developed and experimentally tested. This objective is challenging, since the RWM growth time can vary from a fraction of wall time, that is, a fraction of millisecond, to the angular momentum confinement time, equal to a fraction of second. In addition, the present linear rigid mode growth assumption represents only the dominant mode of several potentially unstable modes. Even this dominant mode may become increasingly nonlinear nearer to the ideal-wall limit. Another important objective is the need to extend RWM stabilization methods to ITER and reactor-oriented devices.

CONTROL OF PLASMA PROFILES AND INTERNAL TRANSPORT BARRIERS

The requirements of ITER and the need to optimize the tokamak concept for designing an economical, possibly steady-state fusion power plant motivate research on plasma transport (see Figure A caption) and confinement in toroidal devices. These investigations have motivated the development of the advanced tokamak (AT) operation scenarios ("Tutorial 13" in [10]) [62] with significantly improved confinement. Experiments in many tokamaks demonstrate the existence of high-performance regimes as quantified by the energy-confinement time and plasma pressure (τ_E and β_N; see "Tutorial 2" in [2]). In these regimes, a dominant fraction of the plasma current is self-generated by the bootstrap mechanism ("Tutorial 21"), which relaxes the requirement for externally driven noninductive current for steady-state operation. This bootstrap current is favored by the generation in the plasma of an internal transport barrier (ITB) [63], a region where particle and heat transport are reduced. An ITB is characterized by large pressure gradients and by the presence of a visible break in the slope of the electron and ion temperature profiles similar to the ETB (see "Tutorial 20"). An ITB is often combined with an ETB, which gives rise to a pressure pedestal at the plasma edge, characteristic of the H-mode [64] ("Tutorial 19").

Although the formation mechanism of ITBs is not entirely known, progress is being made in understanding the ITB. Recent studies show the key influence of the safety factor profile $q(x)$ ($x = r/a$; see "Tutorial 4" and "Tutorial 5" in [2]) for triggering these barriers. Both the radial profile of the magnetic shear ("Tutorial 16" in [1]) and the location of the flux surfaces where q has low-order rational or even integer values are essential for the emergence of ITBs [65]–[67].

When ITBs become too strong, the steep pressure gradient characteristic of the ITB can exceed MHD stability limits, leading to the loss of confinement or to a plasma disruption ("Tutorial 18" in [1]). Thus, steady-state tokamak operation may only be realizable if stationary ITBs can be sustained. This observation has motivated an experimental effort at JET aimed at the real-time simultaneous control of the safety factor, temperature, and pressure profiles. This section reviews the progress achieved based on material in [68]–[72].

Lower hybrid heating and current drive (LHCD; "Tutorial 9" in [7]) is currently used to produce ITBs on JET [73] during the low-density plasma-current-ramp-up phase (see Figure 7 in [2]) prior to the high-performance phase of a discharge in which high-power heating is applied. By using LHCD preheating, certain populations of resonant electrons are unidirectionally

accelerated by electromagnetic waves so that the current density profile ("Tutorial 16" in [1]) is made broader or even hollow, that is, lower at the center than near the edge, depending on the applied power. In this case, the q-profile becomes nonmonotonic in the core of the plasma when the main heating power is applied by ion cyclotron resonance heating (ICRH) and neutral beam injection (NBI) ("Tutorial 9" in [7]). As a result, the magnetic shear changes sign and is said to be reversed.

To control the ITB, it is necessary to characterize it. A local criterion [68] characterizing the location, strength, and dynamics of ITBs in JET can be computed in real time from the ion and electron temperature measurements. This criterion is described in the following section on control of the ITB.

Also described in the next section is a set of experiments that combine ITB control with control of the central plasma pressure. In these experiments, LHCD power plays an important role in preventing the current profile from evolving during the control interval. When LHCD heating is applied in addition to ICRH and NBI during the main heating phase, the LHCD can prevent a preformed broad current profile from changing significantly. Otherwise, the current profile peaks in the plasma center with a characteristic timescale given by the resistive diffusion time (relaxation time of the current profile needed to reach a steady state; "Tutorial 17" in [1]). This peaking tendency is due to the fact that plasma temperature is higher in the core while plasma resistivity ("Tutorial 9" in [7])

Tutorial 21: Bootstrap Current

The bootstrap current is an equilibrium current that is self-generated, without the need of an imposed electric field, in a toroidal plasma. In a tokamak plasma, the guiding centers (the center of the fast Larmor gyro-motion; see Figure 8 in [2]) of most particles follow approximately helical orbits that encircle both the major (vertical) axis of the torus and the magnetic axis of the plasma (see Figure C in Tutorial 1 in [2]). This periodic guiding center motion is a combination of free streaming along the helical magnetic field lines (Figure 9 in [2]) and small radial drifts due to the gradient and curvature of the magnetic field, which average to zero after a complete period. However, the toroidal magnetic field intensity produced by external coils in a tokamak decreases as $1/R$, R being the distance to the major axis, and therefore particles encounter varying field intensities along their orbits, from a minimum $B_{\min}$ on the outer radial part of the helical orbit (the low-field side of the torus) to a maximum $B_{\max}$ on the inner radial part (the high-field side of the torus). As a result, particles with low velocity parallel to the helical field lines, whose kinetic energy W is mainly in the Larmor motion orthogonal to the field lines, cannot complete a helical trajectory around the magnetic axis. Completion of the trajectory violates the conservation of both the energy W and magnetic moment $\mu = W_{\perp}/B$ of the particles along the orbit. At some point in their trajectory, the parallel velocity of the particles vanishes and changes sign. Thus the particles become trapped on the low-field side of the torus where their guiding centers describe banana-shaped orbits (see Figure B). Particles that complete the helical orbit are called passing particles, as opposed to trapped particles. In the presence of a density gradient and at a particular location in the plasma, more trapped particles move in one toroidal direction [trajectory (a) in Figure B] than in the other direction [trajectory (b)], and therefore the local ion and electron velocity distributions are anisotropic. Therefore, each set of trapped particles of a given species passing through a point P carries a finite toroidal momentum proportional to the density gradient at P. Particle collisions give rise to a continuous exchange of momentum between trapped and passing particles. For instance, passing electrons, which make up the bulk of the electron population, receive net toroidal momentum from the anisotropic trapped electrons at an effective rate that is much faster than the rate at which the passing electrons lose momentum to the bulk ions. A net equilibrium electron current results. An additional contribution, with the same sign, comes from the passing ions. This net positive current is known as the bootstrap current.

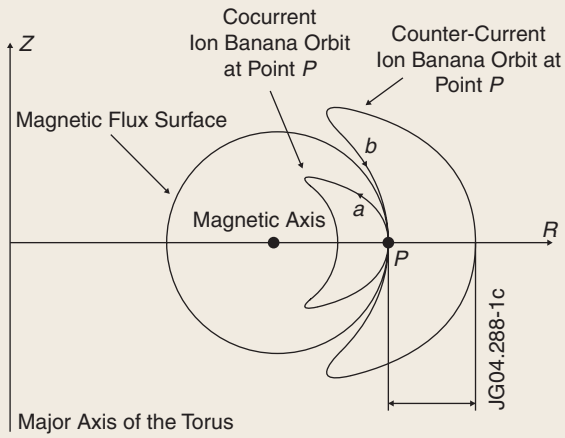

FIGURE B Poloidal projection of two different trapped particle trajectories, also called banana orbits, passing through a point P in the low-field (outer radial) side of the tokamak equatorial plane. The particle trajectories also extend a long way in the toroidal direction around the major axis of the torus when moving from the bottom turning point to the top. The magnetic flux surface passing through the same point is also represented. Trajectory (a) corresponds to an ion that moves toroidally in the co-current direction when passing through point P, whereas trajectory (b) corresponds to an ion that moves toroidally in the counter-current direction at the same location. Due to the increasing density towards the center of the plasma, the number of ions with type (a) orbits is greater than the number of ions with type (b) orbits and thus an anisotropic velocity distribution is sustained at point P.

is inversely related to temperature. The effect of the LHCD is to reduce the current profile peaking [74]. Reduction of this peaking effect helps avoid instabilities or disruptive events related to the presence in the plasma of magnetic flux surfaces with rational q, such as NTMs.

Initial Experiments on ITB Control in JET

The objective of the initial ITB control experiments conducted at JET during 2000–2001 was to investigate practical methods of sustaining ITBs in a controlled and reproducible way. The goal was to tune the applied heating power to maintain the transport barrier and the plasma in a stable state for long periods of time, although not necessarily in steady state. One difficulty in achieving this goal was finding an objective way to satisfactorily quantify the ITB behavior. For that purpose, a local criterion characterizing the presence, location, and strength of ITBs was developed. The criterion is quantified by calculating the ratio ρ_T^* of an ion Larmor radius ρ_i (Figure 8 in [2]) to the temperature gradient scale length $(\nabla T/T)^{-1}$. Using an analysis of an experimental JET database, it is shown in [68] that an ITB is most likely to exist at a normalized radius $x = r/a$ ("Tutorial 5" in [2]) and at time t for which

$$\rho_{\mathrm{T}}^*(\mathbf{x}, \mathbf{t}) \equiv -\rho_{\mathrm{i}} [\nabla \mathbf{T}(\mathbf{x}, \mathbf{t})/\mathbf{T}(\mathbf{x}, \mathbf{t})] > \rho_{\mathrm{ITB}}^*, \tag{8}$$

with the threshold value $\rho_{\mathrm{ITB}}^* \approx 0.014$. (Here, $\nabla T = \partial T/\partial r$.) This criterion enables detection of the presence of an ITB at a given normalized radius with a large degree of confidence when $\rho_T^*(x, t)$ exceeds the fixed threshold value. In JET, transport barriers are usually observed simultaneously in computed values of both the ion temperature gradient ρ_{Ti}^* and the electron temperature gradient ρ_{Te}^* derived from diagnostic measurements. For specificity, we refer to the latter, identified through (8) applied to ρ_{Te}^*, as an electron transport barrier or electron ITB, so that the ITB detection criterion becomes

$$\rho_{Te}^*(x, t) = -\rho_i(\nabla T_e/T_e) > \rho_{\mathrm{ITB}}^*.$$

Electron transport barriers can be controlled using the maximum value of the parameter $\rho_{Te}^*(x, t)$ across the plasma radius as the controlled output variable and with only one power actuator. Best results are obtained when using the ICRH system as the actuator. The temperature measurements from which ρ_{Te}^* is calculated are made with a heterodyne radiometer using the electron cyclotron emission from the plasma [75]. A simple proportional-plus-integral (PI) feedback is used to compute the required actuator input power

$$P(t)[\mathrm{MW}] = P(t_0) + G_p \Delta X(t) + G_I \int_{t_0}^{t} \Delta X(u) du,$$

where $\mathbf{X}(\mathbf{t}) = \max_x[\rho_{\mathbf{Te}}^*(\mathbf{x}, \mathbf{t})]$, $P(t_0)$ is the actuator power at the initial time t_0 of the control, ΔX is the difference between the target output value and the measured output signal $X(t)$, and G_p and G_I and are the proportional and integral gains, respectively. The strategy for controlling the ITB by controlling X using only one actuator, namely, the ICRH heating system, assumes that during the control phase, the current profile (equivalently, q-profile; see "Tutorial 16" in [1]) does not evolve significantly. This simple strategy is thus valid only for periods of time that are shorter than the resistive current diffusion time (greater than or equal to about 10 s in JET). The high power control phases in control experiments are limited to 10 s.

In a second set of experiments [69], the additional effect of a second independent feedback loop to control plasma pressure at the magnetic axis is studied with the aim of combining the ITB confinement improvement with high-β plasma stability to avoid plasma disruptions. Since the neutron production from the deuterium-deuterium (D-D) reactions is strongly correlated with the central plasma pressure, this additional control is achieved by measuring the D-D fusion reaction rate and

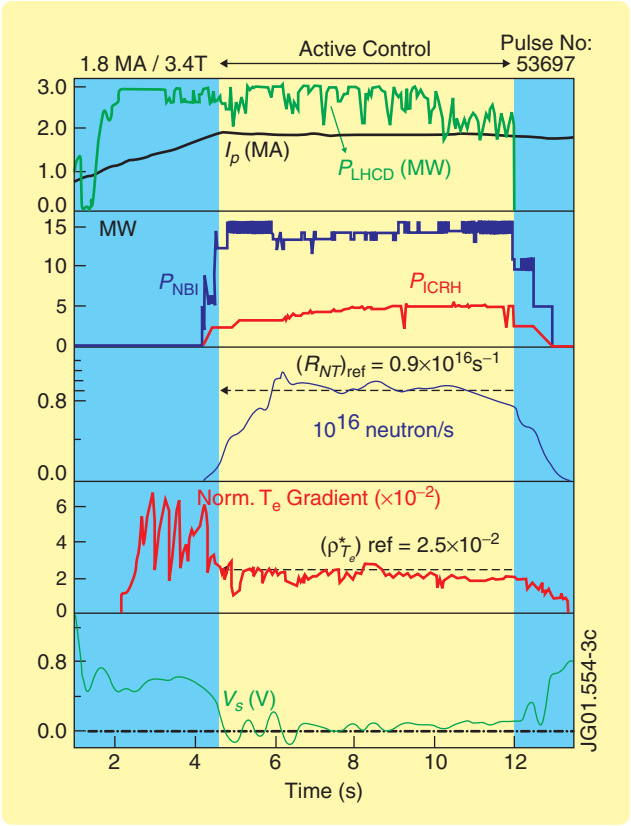

FIGURE 18 Control of an ITB with two single-input, single-output feedback loops [69]. The top two frames show the plasma current I_p as well as the LHCD, NBI, and ICRH heating powers. The values of the maximum normalized electron temperature gradient max$[\rho_{Te}^*]$ (fourth frame) and neutron production rate R_{NT} (third frame) are maintained close to their set points, using ICRH and NBI as actuators respectively. Control starts at 4.5 s, and the set point values are 0.025 for max$[\rho_{Te}^*]$ and 0.9×10^{16} neutrons/s for the neutron production rate. Control of the ITB is sustained for 7.5 s. While the control is applied, the loop voltage V_s (bottom frame) remains close to zero, implying that the current is entirely driven by noninductive sources (Tutorial 9 in [7]), including the self-generated bootstrap current (Tutorial 21). The LHCD power is kept at an approximately constant 3 MW during the control phase to slow down the q-profile relaxation.

We describe control problems associated with instabilities known as neoclassical tearing modes, edge localized modes, and resistive wall modes.

using neutral beam injection (NBI) as the actuator. An experiment with simultaneous control of ρ^*_{Te} with ICRH and of the D-D reaction rate with NBI is depicted in Figure 18 [69]. This control is obtained with a constant 3 MW of LHCD power throughout the pulse, which also demonstrates the important role played by LHCD in slowing down the current density profile evolution (Figure 19), thus improving the long-pulse stationarity of these advanced discharges. Experience suggests that setting up a suitable q-profile, characterized by a weak or reversed magnetic shear, seems to be a key condition for triggering an internal transport barrier that can be controlled to provide the improved plasma confinement. Therefore, to improve the control of the ITB and to allow extended control duration and, later, extrapolation to steady-state burning plasma devices such as ITER, control of the q-profile is required.

Control of the Current Density Profile

The experimental investigations [71], [72] described in this section are the first attempts in JET to control the q-profile. (Controlling the q-profile and the current profile are basically equivalent; see "Tutorial 16" in [1].) The controlled safety factor profile is characterized by its values at five discrete fixed radii, whose values are considered adequate to fully describe the system. The q values are calculated using magnetic measurements together with data from an interferometer-polarimeter diagnostic, which allows a fairly accurate reconstruction (see [7]) of the magnetic equilibrium in real time [70]. The three heating and current drive powers P_{LHCD}, P_{ICRH}, and P_{NBI} are used as actuators for the control. A linearized model is obtained experimentally by performing dedicated open-loop experiments and varying the input powers. A linearized Laplace transform model of the form

$$\delta\mathbf{Q}(s) = \mathbf{K}(s)\delta\mathbf{P}(s). \tag{9}$$

is assumed around a reference plasma steady state, where $\delta\mathbf{Q}$ is a 5×1 vector that represents the change in the safety factor from the reference state when the 3×1 input power vector changes by $\delta\mathbf{P}$. The problem is thus reduced to identifying the 5×3 matrix $\mathbf{K}(s)$ and finding a suitable pseudo-inverse. The steady-state gain matrix $\mathbf{K}(0)$, determined to be sufficient for control, is deduced experimentally from simple power steps relative to the reference state in dedicated open-loop discharges. To design a PI feedback controller that ensures minimum least square steady-state offset, a truncated singular value decomposition of the steady-state gain matrix

$$\mathbf{K}(0) \approx \mathbf{W}\,\Sigma\,\mathbf{V}^T$$

is used [71], retaining two principal components and neglecting a third component having a small singular value. The PI controller transfer function matrix $\mathbf{G}(s)$ is defined by

$$\begin{aligned}\delta\mathbf{P}(s) &= g_c[1 + 1/(\tau_i s)]\mathbf{G}(s)[\delta\mathbf{Q}_{\mathrm{target}} - \delta\mathbf{Q}(s)] \\ &= g_c[1 + 1/(\tau_i s)]\mathbf{V}\Sigma^{-1}\mathbf{W}^T[\delta\mathbf{Q}_{\mathrm{target}} - \delta\mathbf{Q}(s)],\end{aligned}$$

where g_c is the proportional gain and g_c/τ_i is the integral gain.

Because of the long current diffusion timescale, the plasma pulse must be as long as possible to fully assess the effectiveness of the controller. Therefore, a plasma scenario ("Tutorial 13" in [10]) developed for long pulse studies is used. Figure 20 shows the result of a closed-loop experiment in which the q-profile is successfully controlled.

Simultaneous Control of Current and Temperature Gradient Profiles in JET

The demonstration of real-time control of the q-profile motivates new efforts to develop an integrated ITB control, which includes both the current and temperature gradient profiles.

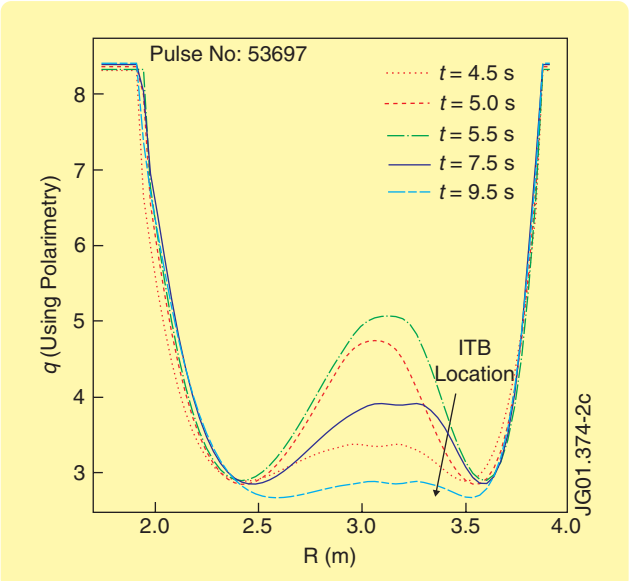

FIGURE 19 Current diffusion process [69]. The time evolution of the q-profile is calculated from a magnetic equilibrium reconstruction code, with LHCD held constant during the high-power heating phase. The q-profile evolution is slow, and in particular the minimum value of q is almost frozen, with a direct effect on the ITB evolution, which is practically stationary around $R = 3.4$ m, where $q \approx 3$ and the magnetic shear is negative. Nevertheless, the current profile continues to evolve slowly. Because of this slow evolution, the simple ITB control shown in Figure 18 cannot be extended to pulse durations longer than the resistive time.

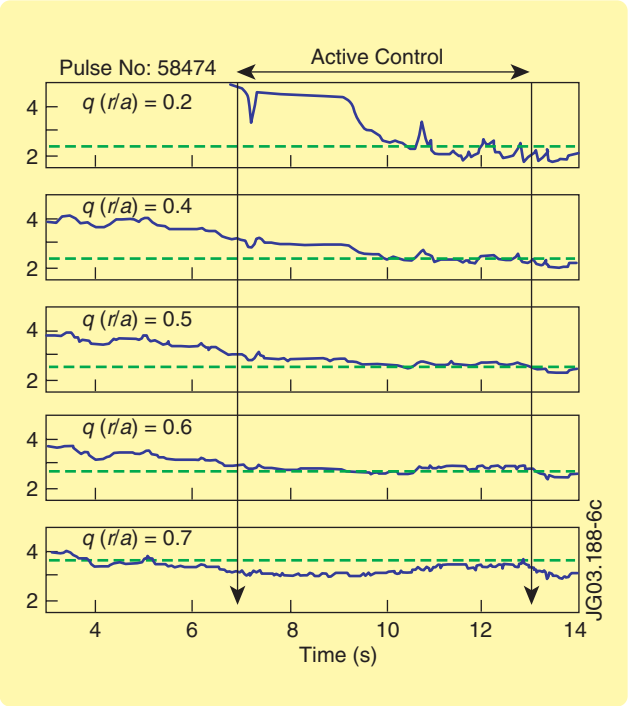

FIGURE 20 A typical example of multiple-input, multiple-output feedback control of the q-profile [71]. Time traces are shown of the safety factor at the five radii selected for the experiment with LHCD, NBI, and ICRH as actuators. The set point values are indicated with dashed lines. The desired set points for $q(x)$ (where $x = r/a$; see Tutorial 5 in [1]) at the five selected radii x = [0.2, 0.4, 0.5, 0.6, 0.8] are q = [2.35, 2.34, 2.44, 2.69, 3.5] and the control is applied between $t = 7$ s and $t = 13$ s. The q-profile had a strong reversed-shear shape at the time when the control starts. The profile then converges slowly toward the profile closest to the request achievable with the given actuators. A transient undershoot occurred between $t \approx 10$s and $t \approx 11$s, and a minimum of the mean square error is reached at $t \approx 12$ s.

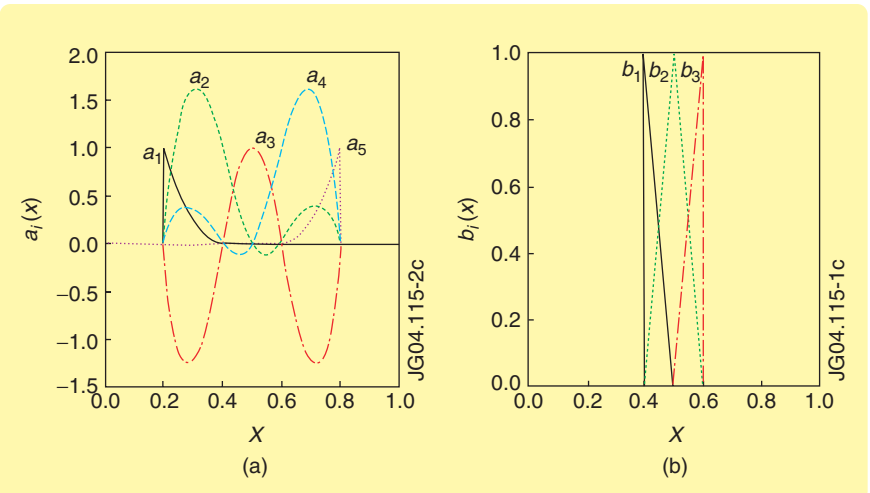

FIGURE 21 Basis functions for the Galerkin projection of (a) ι-profiles (left) and (b) ρ^*_{Te} profiles [72]. (a) Five cubic splines with knots at $x = [0.2, 0.4, 0.5, 0.6, 0.8]$ are used to approximate the ι-profiles. (b) Three triangle functions centered at $x = [0.4, 0.5, 0.6]$ are used to approximate the ρ^*_{Te} profiles by a piecewise linear function in a reduced domain between $x = 0.4$ and $x = 0.6$, where the ITB is requested and controlled.

These two nonlinearly coupled profiles are believed to be essential ingredients governing ITB physics. Recent profile control experiments performed in JET [72] therefore use an extension of the previous model-based technique to simultaneously control $q(x)$ and $\rho^*_{Te}(x)$, both considered as distributed parameters characterizing the current and temperature gradient profiles, respectively.

For this simultaneous control, a discretized representation of the response to the three power inputs NBI, ICRH, and LHCD can be written in the matrix form

$$\delta \mathbf{G}(s) = \mathbf{K}(s)\delta \mathbf{P}(s),$$

similar to (9), and a controller can be derived as described above. The current density profile is represented by $\iota(x)$ because $\iota(x)$, which is directly proportional to the total current in $[0, x]$ ("Tutorial 16" in [1]), depends almost linearly on the applied current drive power while $q(x)$ has an inverse dependence. In the above matrix equation, $\delta G(s) = [G_{\delta\iota_1}(s) \ \ldots \ G_{\delta\iota_{n_a}}(s) \ \ G_{\delta\rho^*_{T_{e1}}}(s) \ \ldots \ G_{\delta\rho^*_{T_{enb}}}(s)]^T$ represents a finite set of coefficients of two sets of basis functions $a_i(x), i = 1, 2, \ldots, n_a$ and $b_i(x), i = 1, 2, \ldots, n_b$ that approximately span the set of achievable $\iota(x)$ and ρ^*_{Te} profiles, respectively [72] (Figure 21). The PI controller structure is defined as

$$\delta \mathbf{P}(s) = g_c\,[1 + 1/(\tau_i s)]\,\mathbf{K}_{\text{inv}}[\delta \mathbf{G}_{\text{target}} - \delta \mathbf{G}(s)], \qquad (10)$$

where g_c is the proportional gain, g_c/τ_i is the integral gain, and $\mathbf{K}_{\text{inv}}$ is a pseudo-inverse of the steady-state gain $\mathbf{K}(0)$.

The real-time controller (10) is used experimentally to control the current density and electron temperature gradient profiles $\rho^*_{Te}(x)$ and obtain an ITB at about half plasma radius. To prevent overloading the real-time controller computation, the number of trial basis functions and the radial windows on which these functions are defined are deliberately limited, that is, only part of the full profiles are controlled. Since the accuracy of the real-time reconstruction of the q-profile from polarimetry data [70] is poor in the central region $0 < x < 0.2$, this region is excluded from the control window. In addition, the q value at the edge is inversely proportional to the total plasma current ("Tutorial 16" in [1]), which is accurately controlled by the primary, ohmic circuit of the tokamak ("Tutorial 9" in [7]). Therefore, including the edge region in the q-profile control is redundant. Thus, feedback control of the q-profile is restricted to the region $0.2 \le x \le 0.8$. For ρ^*_{Te}, the region of control of the

An expert-system-based fault detection system used routinely during DIII-D operations has increased tokamak productivity.

ITB is imposed by limitations in the real-time electron temperature measurements given by the electron cyclotron emission diagnostic, which provides no measurement in either the core of the plasma or near the edge in discharges with LHCD. The radial measurement window depends on the plasma configuration but includes in all cases the region that extends from $x = 0.3$ to $x = 0.7$.

The experiments in [72] had the goal of sustaining an ITB at $x > 0.4$ to enhance the plasma performance. However, q-profiles that are accessible using the present heating systems on JET generally do not allow stationary ITBs at $x \geq 0.6$ to be sustained. Thus, in these experiments the control region for ρ^*_{Te} is restricted to the window $0.4 \leq x \leq 0.6$, where an ITB is expected and requested. The coefficients of both profiles (five coefficients for ι and three for ρ^*_{Te}) are computed online from the profile measurements, and a power request is sent every 10 ms by the controller to the different actuators according to (10). The control scheme is applied in multiple plasma discharges for a maximum of 7 s per discharge and successfully reaches several different target q-profiles, from monotonic to reversed shear, while simultaneously controlling the profile of the electron temperature gradient ρ^*_{Te}. Figure 22 shows the result of applying the control algorithm in the case of a monotonic q-profile target and in the case of a ρ^*_{Te}-profile target with a maximum slightly above the criterion in (8) for the existence of an ITB, at a fairly large ($x = 0.5$) radial location where ITBs are not easily achieved spontaneously. Both profiles are satisfactorily controlled, and the effect of the control can be seen in Figure 23. In this example, the ICRH system fails to deliver the requested power at around $t = 10.25$ s, and therefore the control phase is limited to 4.8 s.

As mentioned in the previous section, the controller defined by (10) minimizes the difference between the target ι and ρ^*_{Te} profiles and their respective real-time measurements, that is, the quadratic error

$$dy^2 = \int_{0.2}^{0.8} \left[\iota(x) - \iota_{\text{setpoint}}(x)\right]^2 dx + \mu \int_{0.4}^{0.6} \left[\rho^*_T(x) - \rho^*_{T_{\text{setpoint}}}(x)\right]^2 dx, \tag{11}$$

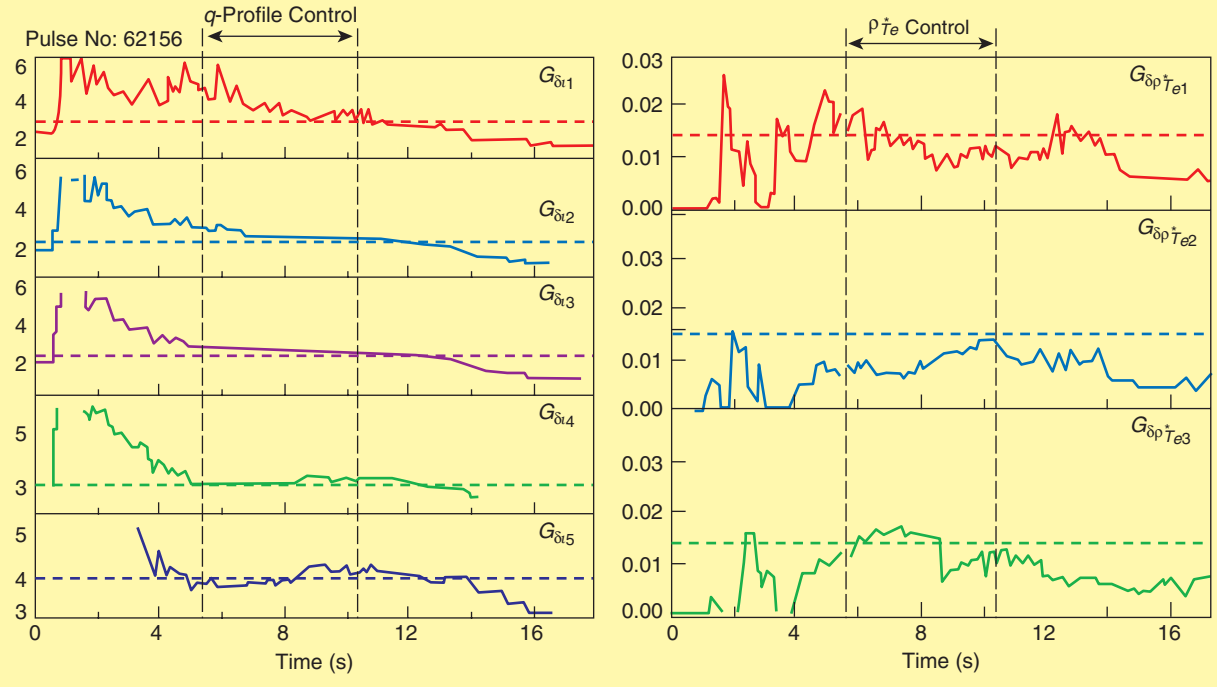

FIGURE 22 A typical example of MIMO control of q and ρ^*_{Te} [72]. Time traces are shown of the Galerkin coefficients defining the (a) q-profile and the (b) ρ^*_{Te} profile during an experiment with LHCD, NBI, and ICRH as actuators for controlling simultaneously the q and ρ^*_{Te} profiles. The set point values are indicated with dashed lines. The control is active between $t = 5.5$ s and $t = 10.25$ s. The target profiles are satisfactorily reached at the end of the control phase despite a strong disturbance causing a perturbation on ρ^*_{Te} ($x = 0.6$) at $t \approx 8.5$ s.

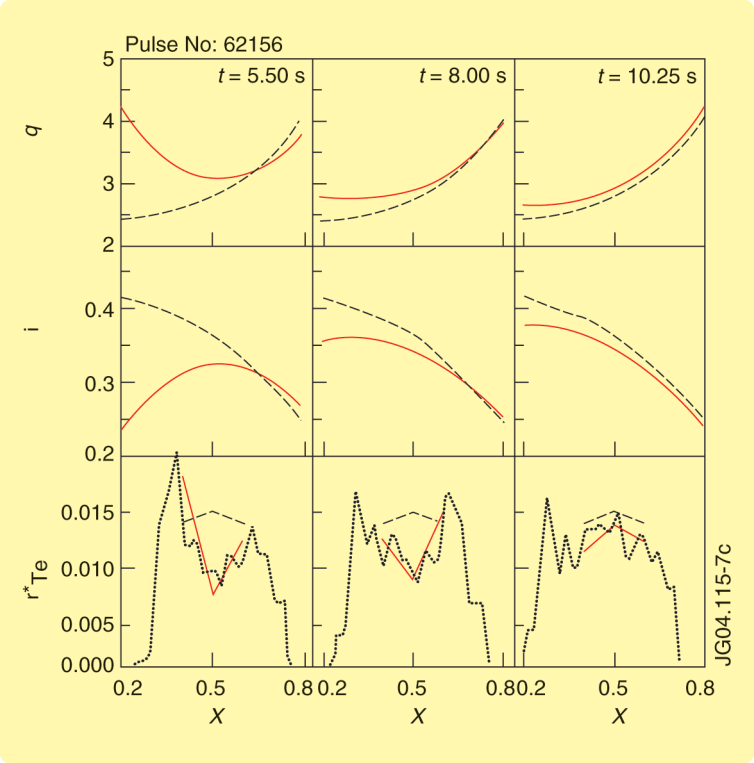

FIGURE 23 Plots of the requested and achieved profiles during the control time window for the pulse number 62156 [72]. Measured profiles (solid) and target profiles (dashed) for q, $\iota = 1/q$, and ρ^*_{Te} are shown after projection onto the span of the basis functions $\{a_i\}_{i=1}^{n_a}$ for ι and $\{b_i\}_{i=1}^{n_b}$ for ρ^*_{Te}. For ρ^*_{Te}, the measured profile before projection is also plotted (dotted). Each column corresponds to one time, respectively, the start of control at $t = 5.5$ s, $t = 8$ s, and end of control at $t = 10.25$ s.

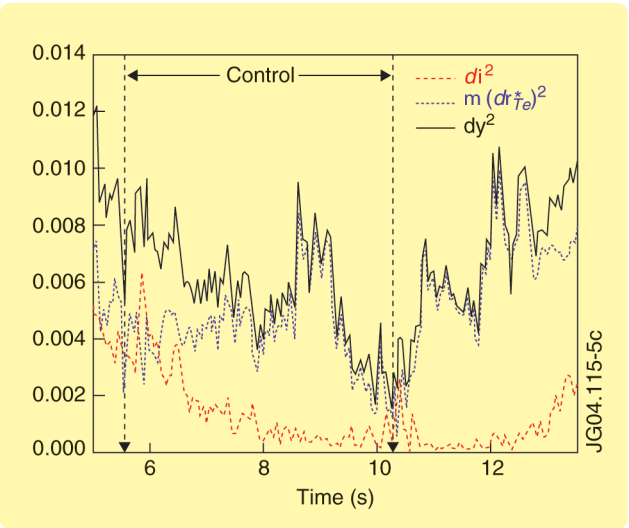

FIGURE 24 Time evolution of the global quadratic error $dy^2 = d\iota^2 + \mu d\rho^{*2}_{Te}$ (solid) defined in (11), and its components $d\iota^2$ (dashed) and $d\rho^{*2}_{Te}$ (dotted) [72]. The effect of the controller minimization is evident from the evolution of the traces after $t = 10.25$ s when the controller action stops because the ICRH system can not deliver the requested power. A large increase of the global distance to the target (solid) can be observed and leads to the loss of the ITB.

where μ is a scalar used for relative weighting of the control objectives. This quantity is plotted in Figure 24. An important feature seen in this experiment is the increase of the error in response to the sudden, undesired failure of the ICRH system to deliver the requested power at $t = 10.25$ s. This failure is immediately followed by a strong rise of the ρ^*_{Te} contribution to the distance to be minimized, showing, by contrast, the effectiveness of the control before the failure of the actuator.

Future Directions

The controllers used at JET for profile control and described in this section are based on knowledge of only the static gain $\mathbf{K}(0)$ of the linear response model $\mathbf{K}(s)$. Experimental identification of a linear dynamic model $\mathbf{K}(s)$ is under investigation to combine the current or q-profile, which evolves on the resistive diffusion timescale, and temperature or pressure profile, which evolves on the energy confinement timescale ("Tutorial 17" in [1]). This combined model can be used to design a controller that can better cope with fast plasma perturbations, such as MHD events or the spontaneous emergence or collapse of ITBs, while converging slowly toward the requested high-performance plasma state. First principles physics models, rather than models identified from data, can be used in future devices to identify adequate linear, or piecewise-linear, response matrices. State-of-the-art plasma transport physics modeling is not accurate enough to provide an adequate model in transient regimes, although it may be useful for a qualitative assessment of the control algorithms [76].

ACKNOWLEDGMENTS

Portions of this work were supported by the U.S. Department of Energy under Contracts DE-FC02-04ER54698 and DE-AC02-76CH03073 and Grant DE-FG02-92ER54141 as well as under the European Fusion Development Agreement (EFDA). We would like to thank A.D. Turnbull for Figure 13, M. Chance for Figure 14, M. Leuer for Figure 10, and P.B. Snyder for Figure 8.

AUTHOR INFORMATION

Michael L. Walker (walker@fusion.gat.com) has been with the fusion group of General Atomics, which operates the DIII-D tokamak under contract to the U.S. Department of Energy, since 1992. He has developed tokamak control systems from initial system modeling through experimental model validation, control design using modern multivariable techniques, implementation in C and assembly language, and incorporation into daily operation of the tokamak. He has also worked in other areas related to control and signal processing,

including development of algorithms, models, and simulations for various electrical, electromagnetic, radio frequency communication, and electromechanical systems. From 1984–1992, he was with General Dynamics, where he developed algorithms and software for signal processing and noncooperative target recognition of military vehicles from radar and infrared data. He can be contacted at General Atomics, P.O. Box 85608, San Diego, CA 92186-5608 USA.

David A. Humphreys earned a Ph.D. in plasma physics from the Massachusetts Institute of Technology (MIT) in 1990, following S.B. degrees in physics and electrical engineering from MIT. He is the group leader of the DIII-D Engineering Physics Group at General Atomics. His current research interests include tokamak stability and disruption physics, complex dynamical systems analysis, electromagnetic field analysis, and multivariable control design. He is the author of numerous technical publications, and has worked in diverse fields from control system design to micro fabrication technology, artificial intelligence, and plasma physics. While at General Atomics, he has studied axisymmetric and nonaxisymmetric MHD physics, including halo currents and other disruption phenomena, poloidal field control, stabilization of RWMs, and suppression of NTMs. As a principal in poloidal field control for the U.S. ITER Home Team, he contributed significantly to the ITER Engineering Design Activity. His theories and models have been successfully applied to many operating devices including JT-60U, JET, Alcator C-MOD, and DIII-D.

Didier Mazon received a Ph.D. degree in physics in the field of energy and combustion from the University of Provence, France. He spent two years with JET at the Culham Science Centre, United Kingdom, where he worked on real-time plasma equilibrium reconstruction, real-time measurement systems, and feedback control of plasma parameters. In 1999, he joined the CEA Cadarache (France), where he is responsible for the Bremsstrahlung emission diagnostics. He works on the development of real-time diagnostics and feedback algorithms for the simultaneous control of the current density and pressure profiles with direct applications in JET and Tore Supra. His research interests include plasma physics, in particular, understanding and control of internal transport barriers, control systems, and transport studies.

Didier Moreau received a degree from Ecole Centrale des Arts et Manufactures, France, in 1974, an M.S.E. degree from Princeton University in 1976, and the Habilitation à Diriger des Recherches from the Université de Provence, France, in 1993. He is an "expert senior" researcher at the Commissariat à l'Energie Atomique, France, and a professor at the Institut National des Sciences et Techniques Nucléaires, France. He received the rank of Chevalier de l'Ordre des Palmes Académiques in 2003. He has been a researcher in magnetic fusion since 1976 (CEA with detachments at JET Joint Undertaking and EFDA-JET). His main interests are plasma waves, plasma heating and current drive, and advanced scenarios and plasma control for high-performance steady-state operation of tokamaks.

Michio Okabayashi received his master's and Ph.D. degrees in physics from the University of Tokyo in 1965 and 1968, respectively. Since then, he has been with the Princeton Plasma Physics Laboratory, where he has been involved in fusion plasma physics research for fusion devices, including the Princeton tokamaks PDX, PBX(-M), and TFTR. From 1981–1985 he was head of the Physics Group for the Princeton Beta Experiment (PBX) and the Modified Princeton Beta Experiment (PBX-M). He is the coordinator of the multi-institutional resistive wall mode research effort at the DIII-D tokamak. Dr. Okabayashi has been a fellow of the American Physical Society since 1983.

Thomas H. Osborne earned his Ph.D. in physics from the University of Wisconsin, Madison, in 1984, at which time he joined General Atomics to work in the MHD stability and physics operations group of DIII-D. He developed many of the plasma shape control algorithms initially used on DIII-D and in the current digital shape control system. His main area of research has been H-mode physics. Dr. Osborne was cochair of the Pedestal Topical Group of the International Tokamak Physics Activity (ITPA) until 2003.

Eugenio Schuster is an assistant professor in the Department of Mechanical Engineering and Mechanics at Lehigh University. He holds undergraduate degrees in electronic engineering (Buenos Aires University, Argentina, 1993) and nuclear engineering (Balseiro Institute, Argentina, 1998). He obtained his M.Sc. (2000) and Ph.D. (2004) degrees in mechanical and aerospace engineering from the University of California San Diego, with Miroslav Krstic as his advisor. His research interests include finite-dimensional and distributed-parameter nonlinear control theory, and its application to complex physical systems such as fusion reactors, plasmas, magnetohydrodynamic flows, and particle accelerators. He is member of the IEEE, ASME, and ANS.

REFERENCES

[1] G. Ambrosino and R. Albanese, "Magnetic control of plasma current, position, and shape in tokamaks: A survey of modeling and control approaches," *Control Syst. Mag.*, vol. 25, no. 5, pp. 76–92, Oct. 2005.

[2] A. Pironti and M.L. Walker, "Fusion, tokamaks, and plasma control: An introduction and tutorial," *Control Syst. Mag.*, vol. 25, no. 5, pp. 30–43, Oct. 2005.

[3] Z. Chang, J.D. Callen, E.D. Fredrickson, R.V. Budny, C.C. Hegna, K.M. McGuire, and M.C. Zarnstorff, "Observation of nonlinear neoclassical pressure-gradient-driven tearing modes in TFTR," *Phys. Rev. Lett.*, vol. 74, no. 23, p. 4663, 1995.

[4] R.J. Buttery, T.C. Hender, D.F. Howell, R.J. La Haye, O. Sauter, D. Testa, and contributors to the EFDA-JET Workprogramme, "Onset of neoclassical tearing modes on JET," *Nucl. Fusion*, vol. 43, no. 2, p. 69, 2003.

[5] D.P. Brennan, R.J. La Haye, A.D. Turnbull, M.S. Chu, T.H. Jensen, L.L. Lao, T.C. Luce, P.A. Politzer, E.J. Strait, S.E. Kruger, and D.D. Schnack, "A mechanism for tearing onset near ideal stability boundaries," *Phys. Plasmas*, vol. 10, no. 5, p. 1643, 2003.

[6] R.J. La Haye, S. Gunter, D.A. Humphreys, J. Lohr, T.C. Luce, M.E. Maraschek, C.C. Petty, R. Prater, J.T. Scoville, and E.J. Strait, "Control of neoclassical tearing modes in DIII-D," *Phys. Plasmas*, vol. 9, no. 5, p. 2051, 2002.

[7] A. Beghi and A. Cenedese, "Advances in real-time plasma boundary reconstruction: From gaps to snakes," *IEEE Control Syst. Mag.*, vol. 25, no. 5, pp. 44–64, Oct. 2005.

[8] R.W. Callis, J. Lohr, D. Ponce, T.E. Harris, R.C. O'Neill, D.B. Remsen, R. Prater, and T.C. Luce, "3 MW, 110 GHz ECH system for the DIII-D tokamak," in *Proc. 20th Symp. Fusion Technology, Marseille, France*, 1998, vol. 1, p. 315.
[9] K. Nagasaki, A. Isayama, S. Ide, and JT-60 team, "Stabilization effect of early ECCD on a neoclassical tearing mode in the JT-60U tokamak," *Nucl. Fusion*, vol. 43, no. 10, p. L7, 2003.
[10] M. Ariola and A. Pironti, "Plasma shape control for the JET tokamak: An optimal output regulation approach," *Control Syst. Mag.*, vol. 25, no. 5, pp. 65–75, Oct. 2005.
[11] R.J. La Haye, T.C. Luce, C.C. Petty, D.A. Humphreys, A.W. Hyatt, F.W. Perkins, R. Prater, E.J. Strait, and M.R. Wade, "Complete suppression of the m/n=2/1 neoclassical tearing mode using radially localized electron cyclotron current drive on DIII-D and the requirements for ITER," in *Proc. 30th EPS Conf. Control Fusion and Plasma Physics*, St. Petersburg, Russia, 2003, vol. 27A, P-2.109.
[12] B.W. Rice, "q-profile measurements with the motional Stark effect diagnostic in the DIII-D tokamak," *Fus. Eng. Design (Special issue on fusion plasma diagnostics)*, vol. 34–35, pp. 135–142, 1997.
[13] ITER [FEAT], "Final design report (FDR), plant description documents, chapter 5, safety" [Online. Available: http://web.gat.com/iter-fdr/final-report-sep-2001/ Plant_Descptn_Docs_(PDDs)/PDD_5_Safety.pdf
[14] ITER [FEAT], "Final design report (FDR), plant description documents, chapter 3, section 7, control" [Online]. Available: http://web.gat.com/iter-fdr/final-report-sep-2001/Plant_Descptn_Docs_(PDDs)/PDD_3.7_ Control.pdf
[15] D. Wróblewski, G.L. Jahns, and J.A. Leuer, "Tokamak disruption alarm based on a neural network model of the high-β limit," *Nucl. Fus.*, vol. 37, no. 6, p. 725, 1997.
[16] M.K. Zedda, T. Bolzonella, B. Cannas, A. Fanni, D. Howell, M.F. Johnson, and P. Sonato, "Disruption classification at JET with neural techniques," in *Proc. 30th EPS Conf. Controlled Fusion and Plasma Physics*, St. Petersburg, Russia, 2003, vol. 27A, P-2.93.
[17] G. Pautasso, C. Tichmann, S. Egorov, T. Zehetbauer, O. Gruber, M. Maraschek, K.-F. Mast, V. Mertens, I. Perchermeier, G. Raupp, W. Treutterer, C.G. Windsor, and ASDEX Upgrade Team, "On-line prediction and mitigation of disruptions in ASDEX Upgrade," *Nucl. Fusion*, vol. 42, p. 100, 2002.
[18] F.C. Morabito, M. Versaci, G. Pautasso, C. Tichmann, ASDEX Upgrade Team, "Fuzzi-Neural approaches to the prediction of disruptions in ASDEX-Upgrade," *Nucl. Fusion*, vol. 40, no. 11, p. 1715, 2001.
[19] S.C. Jardin, G.L. Schmidt, E.D. Fredrickson, K.W. Hill, J. Hyuna, B.J. Merrill, and R. Sayer, "A fast shutdown technique for large tokamaks," *Nucl. Fusion*, vol. 40, no. 5, p. 923, 2000.
[20] D.G. Whyte, T.C. Jernigan, D.A. Humphreys, A.W. Hyatt, C.J. Lasnier, P.B. Parks, T.E. Evans, M.N. Rosenbluth, P.L. Taylor, A.G. Kellman, D.S. Gray, and E.M. Hollmann, "Mitigation of tokamak disruptions using high-pressure gas injection," *Phys. Rev. Lett.*, vol. 89, no. 5, p. 055001–1, 2002.
[21] A. Rizzo and M.G. Xibilia, "An innovative intelligent system for sensor validation in tokamak machines," *IEEE Trans. Contr. Syst. Technol.*, vol. 10, no. 3, p. 421, 2002.
[22] L. Fortuna, V. Marchese, A. Rizzo, and M.G. Xibilia, "A neural networks based system for post pulse fault detection and disruption data validation in tokamak machines," in *Proc. 1999 IEEE Int. Symp. Circuits and Systems*, 1999, vol. 5, p. 563.
[23] M.L. Walker, J.T. Scoville, R.D. Johnson, A.W. Hyatt, and J. Lee, "Automated fault detection for DIII-D tokamak experiments," in *Proc. 18th IEEE/NPSS Symp. Fusion Engineering*, Piscataway, NJ, 1999, p. 539.
[24] P.M. Frank, "Fault diagnosis in dynamic systems using analytical and knowledge-based redundancy—A survey and some new results," *Automatica*, vol. 26, no. 3, p. 459, 1990.
[25] R. Isserman and P. Balle, "Trends in the application of model-based fault detection and diagnosis of technical processes," *Control Eng. Practice*, vol. 5, no. 5, p. 709, 1997.
[26] J.C. Giarratano and G. Riley, *Expert Systems Principles and Programming*. Boston, MA: PWS-Kent, 1998.
[27] E. Jotaki and S. Itoh, "A data acquisition method against unpredictable events during long-time discharges and its application to the TRIAM-1M tokamak experiment," *Fusion Tech.*, vol. 32, no. 3, p. 487, 1997.
[28] K. Blackler and A.W. Edwards, "The JET fast central acquisition and trigger system," EFDA-JET, Culham Science Centre, Abingdon, Oxfordshire, UK, Rep. JET-P(93) 49, 1993.
[29] V. Mertens, G. Raupp, and W. Treutterer, "Plasma control in ASDEX Upgrade," *Fusion Sci. Tech.*, vol. 44, no. 3, p. 593, 2003.
[30] H. Zohm, "Edge localized modes (ELMs)," *Plasma Phys. Contr. Fusion*, vol. 38, no. 2, pp. 105–128, 1996.
[31] R.J. Groebner, "An emerging understanding of H-mode discharges in tokamaks," *Phys. Fluids B*, vol. 5, no. 7, p. 2343, 1993.
[32] G. Federici, A. Loarte, and G. Strohmayer, "Assessment of erosion of the ITER divertor targets during type I ELMs," *Plasma Phys. Contr. Fusion*, vol. 45, no. 9, pp. 1523–1547, 2003.
[33] P.B. Snyder, H.R. Wilson, and X.Q. Xu, "Progress in the peeling-ballooning model of ELMs: Numerical studies of nonlinear dynamics," *Phys. Plasmas*, vol. 12, no. 5, p. 056115-1, 2005.
[34] P.T. Lang, "Active edge localized mode (ELM) frequency control with pellets," in *Proc. 30th EPS Conf. Control Fusion and Plasma Physics*, St. Petersburg, Russia, 2003, vol. 27A, p. 1.129.
[35] A.W. Degeling, "Magnetic triggering of ELMs in TCV," in *Proc. 30th EPS Conf. Control Fusion and Plasma Physics*, St. Petersburg, Russia, 2003, vol. 27A, p. 3.128.
[36] M. Greenwald, R. Boivin, P. Bonoli, C. Fiore, J. Goetz, R. Granetz, A. Hubbard, I. Hutchinson, J. Irby, Y. Lin, E. Marmar, A. Mazurenko, D. Mossessian, T. Sunn Pedersen, J. Rice, J. Snipes, G. Schilling, G. Taylor, J. Terry, S. Wolfe, and S. Wukitch, "Studies of EDA H-mode in Alcator C-Mod," *Plasma Phys. Contr. Fusion*, vol. 42, suppl. 5A, pp. A263–A269, 2000.
[37] K. Kamiya, H. Kimura, H. Ogawa, H. Kawashima, K. Tsuzuki, M. Sato, Y. Miura, and JFT-2M group, "Observation of high recycling steady H-mode edge and compatibility with improved core confinement mode on JFT-2M," *Nucl. Fusion*, vol. 43, no. 10, pp. 1214–1219, 2003.
[38] K.H. Burrell, M.E. Austin, D.P. Brennan, J.C. DeBoo, E.J. Doyle, P. Gohil, C.M. Greenfield, R.J. Groebner, L.L. Lao, T.C. Luce, M.A. Makowski, G.R. McKee, R.A. Moyer, T.H. Osborne, M. Porkolab, T.L. Rhodes, J.C. Rost, M.J. Schaffer, B.W. Stallard, E.J. Strait, M.R. Wade, G. Wang, J.G. Watkins, W.P. West, and L. Zeng, "Quiescent high confinement mode plasmas in the DIII-D tokamak," *Plasma Phys. Contr. Fusion*, vol. 44, no. 5A, pp. A253–A263, 2002.
[39] K.H. Burrell, M.E. Austin, D.P. Brennan, J.C. DeBoo, E.J. Doyle, C. Fenzi, C. Fuchs, P. Gohil, C.M. Greenfield, R.J. Groebner, L.L. Lao, T.C. Luce, M.A. Makowski, G.R. McKee, R.A. Moyer, C.C. Petty, M. Porkolab, C.L. Rettig, T.L. Rhodes, J.C. Rost, B.W. Stallard, E.J. Strait, E.J. Synakowski, M.R. Wade, J.G. Watkins, and W.P. West, "Quiescent double barrier high confinement mode plasmas in the DIII-D tokamak," *Phys. Plasmas*, vol. 8, no. 5, p. 2153, 2001.
[40] W. Suttrop, G.D. Conway, L. Fattorini, L.D. Horton, T. Kurki-Suonio, C.F. Maggi, M. Maraschek, H. Meister, R. Neu, Th. Pütterich, M. Reich, A.C.C. Sips, and the ASDEX Upgrade Team, "Stationary ELM-free H-mode in ASDEX upgrade," *Plasma Phys. Contr. Fusion*, vol. 46, no. 5A, p. A151, 2004.
[41] T.E. Evans, R.A. Moyer, P.R. Thomas, J.G. Watkins, T.H. Osborne, J.A. Boedo, E.J. Doyle, M.E. Fenstermacher, K.H. Finken, R.J. Groebner, M. Groth, J.H. Harris, R.J. La Haye, C.J. Lasnier, S. Masuzaki, N. Ohyabu, D.G. Pretty, T.L. Rhodes, H. Reimerdes, D.L. Rudakov, M.J. Schaffer, G. Wang, and L. Zeng, *Phys. Rev. Lett.*, vol. 92, no. 23, p. 235003-1, 2004.
[42] T.E. Evans, R.A. Moyer, J.G. Watkins, T.H. Osborne, P.R. Thomas, M. Becoulet, J.A. Boedo, E.J. Doyle, M.E. Fenstermacher, K.H. Finken, R.J. Groebner, M. Groth, J.H. Harris, G.L. Jackson, R.J. La Haye, C.J. Lasnier, S. Masuzaki, N. Ohyabu, D.G. Pretty, H. Reimerdes, T.L. Rhodes, D.L. Rudakov, M.J. Schaffer, M.R. Wade, G. Wang, W.P. West, and L. Zeng, *Nucl. Fusion 45*, no. 7, p. 595, 2005.
[43] R. Aymar, Y. Shimomura, M. Huguet, V. Chuyanov, ITER international and participant teams., "ITER: Fusion research at the dawn of a new era," in *Proc. 19th IAEA Fusion Conf.*, Lyon, France, Oct. 14–19, 2002, p. OV1/1.
[44] L.C. Bernard, F.J. Helton, and R.W. Moore, "GATO: An ideal MHD stability code for axisymmetric plasmas with internal separatrices," *Comput. Phys. Commun.*, vol. 24, no. 3-4, p. 377, 1981.
[45] T.S. Taylor, H. St John, A.D. Turnbull, V.R. Lin-Liu, K.H. Burrell, V. Chan, M.S. Chu, J.R. Ferron, L.L. Lao, R.J. La Haye, E.A. Lazarus, R.L. Miller, P.A. Politzer, D.P. Schissel, E.J. Strait, "Optimized profiles for improved confinement and stability in the DIII-D tokamak," *Plasma Phys. Contr. Fusion*, vol. 36, no. 12B, p. B229, 1994.
[46] M. Okabayashi, N. Pomphrey, J. Manickam, D.J. Ward, R.E. Bell, R.E. Hatcher, R. Kaita, S.M. Kaye, H.W. Kugel, B. LeBlanc, F.M. Levinton, D.W. Roberts, S. Sesnic, Y. Sun, and H. Takahashi, "Role of the stabilizing shell in high-beta, low-q disruptions in PBX-M," *Nucl. Fusion*, vol. 36, no. 9, p. 1167, 1996.
[47] A.M. Garofalo, T.H. Jensen, L.C. Johnson, R.J. La Haye, G.A. Navratil, M. Okabayashi, J.T. Scoville, E.J. Strait, D.R. Baker, J. Bialek, M.S. Chu, J.R. Ferron, J. Jayakumar, L.L. Lao, M.A. Makowski, H. Reimerdes, T.S. Taylor, A.D. Turnbull, M.R. Wade, and S.K. Wong, "Sustained rotational stabilization of DIII-D plasmas above the no-wall beta limit," *Phys. Plasmas*, vol. 9, no. 5, p. 1997, 2002.

[48] S. Takeji, S. Tokuda, T. Fujita, T. Suzuki, A. Isayama, S. Ide, Y. Ishii, Y. Kamada, Y. Koide, T. Matsumoto, T. Oikawa, T. Ozeki, Y. Sakamoto, and JT-60 Team, "Resistive instabilities in reversed shear discharges and wall stabilization on JT-60U," *Nucl. Fusion*, vol. 42, no. 1, p. 5, 2002.

[49] M. Okabayashi, J. Bialek, M.S. Chance, M.S. Chu, E.D. Fredrickson, A.M. Garofalo, R. Hatcher, T.H. Jensen, L.C. Johnson, R.J. La Haye, G.A. Navratil, H. Reimerdes, J.T. Scoville, E.J. Strait, A.D. Turnbull, M.L. Walker, and the DIII-D Team, "Stabilization of the resistive wall mode in DIII-D by plasma rotation and magnetic feedback," *Plasma Phys. Contr. Fusion*, vol. 44, no. 12B, p. B339, 2002.

[50] E.J. Strait, J.M. Bialek, I.N. Bogatu, M.S. Chance, M.S. Chu, D.H. Edgell, A.M. Garofalo, G.L. Jackson, R.J. Jayakumar, T.H. Jensen, O. Katsuro-Hopkins, J.S. Kim, R.J. La Haye, L.L. Lao, M.A. Makowski, G.A. Navratil, M. Okabayashi, H. Reimerdes, J.T. Scoville, A.D. Turnbull, and DIII-D Team, "Resistive wall mode stabilization with internal feedback coils in DIII-D," *Phys. Plasmas*, vol. 11, no. 5, p. 2505, 2004.

[51] M. Okabayashi, N. Pomphrey, and R.E. Hatcher, "Circuit equation formulation of resistive wall mode feedback stabilization schemes," *Nucl. Fusion*, vol. 38, no. 11, p. 1607, 1998.

[52] A.H. Boozer, "Equations for studies of feedback stabilization," *Phys. Plasmas*, vol. 5, no. 9, p. 3350, 1998.

[53] Y.Q. Liu, A. Bondeson, "Active feedback stabilization of toroidal external modes in tokamaks," *Phys. Rev. Lett.*, vol. 84, no. 5, p. 907, 2000.

[54] M.S. Chu, V.S. Chan, M.S. Chance, D.H. Edgell, A.M. Garofalo, A.H. Glasser, S.C. Guo, D.A. Humphreys, T.H. Jensen, J.S. Kim, R.J. La Haye, L. Lao, G.A. Navratil, M. Okabayashi, F.W. Perkins, H. Reimerdes, H.E. St. John, E. Soon, E.J. Strait, A.D. Turnbull, M.L. Walker, and S.K. Wong, "Modeling of feedback and rotation stabilization of the resistive wall mode in tokamaks," *Nucl. Fusion*, vol. 43, no. 3, pp. 196–201, 2003.

[55] D.H. Edgell, J.S. Kim, I.N. Bogatu, D.A. Humphreys, A.D. Turnbull, "Magnetohydrodynamic mode identification from magnetic probe signals via a matched filter method," *Rev. Sci. Instrum.*, vol. 73, no. 4, p. 1761, 2002.

[56] C.M. Fransson, D.H. Edgell, D.A. Humphreys, and M.L. Walker, "Model validation, dynamic edge location mode discrimination, and high confidence resistive wall mode control in DIII-D," *Phys. Plasmas*, vol. 10, no. 10, pp. 3961–3974, 2003.

[57] C.M. Fransson, B. Lennartson, C. Breitholtz, A. Bondeson, Y.Q. Liu, "Feedback stabilization of nonaxisymmetric resistive wall modes in tokamaks, II. Control Analysis," *Phys. Plasmas*, vol. 7, no. 10, pp. 4143–4151, 2000.

[58] A. Bondeson, Y. Liu, C.M. Fransson, B. Lennartson, C. Breitholtz, and T.S. Taylor, "Active feedback stabilization of high beta modes in advanced tokamaks," *Nucl. Fusion*, vol. 41, no. 4, p. 455, 2001.

[59] M. Okabayashi, J. Bialek, M.S. Chance, M.S. Chu, E.D. Fredrickson, A.M. Garofalo, M. Gryaznevich, R.E. Hatcher, T.H. Jensen, L.C. Johnson, R.J. La Haye, E.A. Lazarus, M.A. Makowski, J. Manickam, G.A. Navratil, J.T. Scoville, E.J. Strait, A.D. Turnbull, and M.L. Walker, "Active feedback stabilization of the resistive wall mode on the DIII-D device," *Phys. Plasmas*, vol. 8, no. 5, p. 2071, 2001.

[60] J. Bialek, A.H. Boozer, M.E. Mauel, and G.A. Navratil, "Modeling of active control of external magnetohydrodynamic instabilities," *Phys. Plasmas*, vol. 8, no. 5, p. 2170, 2001.

[61] M.S. Chu, A. Bondeson, M.S. Chance, Y.Q. Liu, A.M. Garofalo, A.H. Glasser, G.L. Jackson, R.J. La Haye, L.L. Lao, G.A. Navratil, M. Okabayashi, H. Remierdes, J.T. Scoville, and E.J. Strait, "Modeling of feedback stabilization of resistive wall mode in rotating plasmas," *Phys. Plasmas*, vol. 11, no. 5, p. 2497, 2004.

[62] T.S. Taylor, "Physics of advanced tokamaks," *Plasma Phys. Control. Fusion*, vol. 39, no. 12B, p. B47, 1997.

[63] J. Connor, T. Fukuda, X. Garbet, C. Gormezano, V. Mukhovatov, M. Wakatani, the ITB Database Group, the ITPA Topical Group on Transport and Internal Barrier Physics, "A review of internal transport barrier physics for steady state operation of tokamaks," *Nucl. Fusion*, vol. 44, no. 4, p. R1, 2004.

[64] F. Wagner, G. Becker, K. Behringer, D. Campbell, A. Eberhagen, W. Engelhardt, G. Fussmann, O. Gehre, J. Gernhardt, G.V. Gierke, G. Haas, M. Huang*, F. Karger, M. Keilhacker, O. Klüber, M. Kornherr, K. Lackner, G. Lisitano, G.G. Lister, H.M. Mayer, D. Meisel, E.R. Müller, H. Murmann, H. Niedermeyer, W. Poschenrieder, H. Rapp, H. Röhr, F. Schneider, G. Siller, E. Speth, A. Stäbler, K.H. Steuer, G. Venus, O. Vollmer, and Z. Yü, "Regime of improved confinement and high beta in neutral beam heated divertor discharges of the ASDEX tokamak," *Phys. Rev. Lett.*, vol. 49, no. 19, p. 1408, 1982.

[65] T.J.J. Tala, J.A. Heikkinen, V.V. Parail, Yu F. Baranov, and S.J. Karttunen, "ITB formation in terms of $\omega_{E\times B}$ flow shear and magnetic shear on JET," *Plasma Phys. Contr. Fusion*, vol. 43, no. 4, p. 507, 2001.

[66] E. Joffrin, G. Gorini, C.D. Challis, N.C. Hawkes, T.C. Hender, D.F. Howell, P. Maget, P. Mantica, D. Mazon, S.E. Sharapov, G. Tresset, and contributors to the EFDA-JET Workprogramme, "Triggering of internal transport barrier in JET," *Plasma Phys. Contr. Fusion*, vol. 44, no. 8, p. 1739, 2002.

[67] X. Garbet, Y. Baranov, G. Bateman, S. Benkadda, P. Beyer, R. Budny, F. Crisanti, B. Esposito, C. Figarella, C. Fourment, P. Ghendrih, F. Imbeaux, E. Joffrin, J. Kinsey, A. Kritz, X. Litaudon, P. Maget, P. Mantica, D. Moreau, Y. Sarazin, A. Pankin, V. Parail, A. Peeters, T. Tala, G. Tardini, A. Thyagaraja, I. Voitsekhovitch, J. Weiland, R. Wolf, and JET EFDA contributors, "Micro stability and transport modelling of internal transport barriers on JET," *Nucl. Fusion*, vol. 43, no. 9, p. 975, 2003.

[68] G. Tresset, X. Litaudon, D. Moreau, X. Garbet, and Contributors to the EFDA-JET Work Programme, "A dimensionless criterion for characterising internal transport barriers in JET," *Nucl. Fusion*, vol. 42, no. 5, p. 520, 2002.

[69] D. Mazon, X. Litaudon, D. Moreau, M. Riva, G. Tresset, Y. Baranov, A. Bécoulet, J.M. Chareau, F. Crisanti, R. Dux, R. Felton, E. Joffrin, and contributors to the EFDA-JET workprogramme, "Real-time control of internal transport barriers in JET," *Plasma Phys. Contr. Fusion*, vol. 44, no. 7, p. 1087, 2002.

[70] L. Zabeo, A. Murari, E. Joffrin, D. Mazon, and C. Taliercio, "A versatile method for the real-time determination of the safety factor and density profiles in JET," *Plasma Phys. Contr. Fusion*, vol. 44, no. 11, p. 2483, 2002.

[71] D. Moreau, F. Crisanti, X. Litaudon, D. Mazon, P. De Vries, R. Felton, E. Joffrin, L. Laborde, M. Lennholm, A. Murari, V. Pericoli-Ridolfini, M. Riva, T. Tala, G. Tresset, L. Zabeo, K.D. Zastrow, and contributors to the EFDA-JET Workprogramme, "Real-time control of the q-profile in JET for steady state advanced tokamak operation," *Nucl. Fusion*, vol. 43, no. 9, p. 870, 2003.

[72] L. Laborde, D. Mazon, D. Moreau, A. Murari, R. Felton, L. Zabeo, R. Albanese, M. Ariola, J. Bucalossi, F. Crisanti, M. de Baar, G. de Tommasi, P. de Vries, E. Joffrin, M. Lennholm, X. Litaudon, A. Pironti, T. Tala, and A. Tuccillo, "A model-based technique for real-time control of current and pressure profiles in the JET tokamak," *Plasma Phys. Contr. Fusion*, vol. 47, no. 1, p. 155, 2005.

[73] C.D. Challis, Yu.F. Baranov, G.D. Conway, C. Gormezano, C.W. Gowers, N.C. Hawkes, T.C. Hender, E. Joffrin, J. Mailloux, D. Mazon, S. Podda, R. Prentice, F.G. Rimini, S.E. Sharapov, A.C.C. Sips, B.C. Stratton, D. Testa, and K.-D. Zastrow, "Effect of q-profile modification by LHCD on internal transport barriers in JET," *Plasma Phys. Contr. Fusion*, vol. 43, no. 7, p. 861, 2001.

[74] X. Litaudon, F. Crisanti, B. Alper, J.F. Artaud, Yu.F. Baranov, E. Barbato, V. Basiuk, A. Bécoulet, M. Bécoulet, C. Castaldo, C.D. Challis, G.D. Conway, R. Dux, L.G. Eriksson, B. Esposito, C. Fourment, D. Frigione, X. Garbet, C. Giroud, N.C. Hawkes, P. Hennequin, G.T.A. Huysmans, F. Imbeaux, E. Joffrin, P.J. Lomas, Ph. Lotte, P. Maget, M. Mantsinen, J. Mailloux, D. Mazon, F. Milani, D. Moreau, V. Parail, E. Pohn, F.G. Rimini, Y. Sarazin, G. Tresset, K.D. Zastrow, M. Zerbini, and contributors to the EFDA-JET Workprogramme, "Towards fully non-inductive current drive operation in JET," *Plasma Phys. Contr. Fusion*, vol. 44, no. 7, p. 1057, 2002.

[75] E. De la Luna, P. Blanchard, A. Bruschi, C. Cientioli, G. Conway, R. Felton, J. Fessey, C. Gowers, E. Joffrin, D. Mazon, A. Murari, S. Nowak, M. Riva, A. Simonetto, C. Sozzi, J. Sanchez, M. Zerbini, and JET-EFDA contributors, "Recent developments of ECE diagnostics at JET," in *Proc. 13th Joint Workshop on ECE and ECRH 2004* [Online]. Available: http://www.ec13.iapras.ru/on-line-papers. htm and E. Joffrin, F. Crisanti, R. Felton, X. Litaudon, D. Mazon, D. Moreau, L. Zabeo, R. Albanese, M. Ariola, D. Alves, O. Barana, V. Basiuk, A. Bécoulet, M. Bécoulet, J. Blum, T. Bolzonnella, K. Bosak, J.M. Chareau, M. de Baar, E. de la Luna, P. de Vries, P. Dumortier, D. Elbeze, J. Farthing, H. Fernandes, C. Fenzi, R. Giannella, K. Guenther, J. Harling, N. Hawkes, T.C. Hender, D.F. Howell, P. Heesterman, F. Imbeaux, P. Innocente, L. Laborde, G. Lloyd, P.J. Lomas, D.C. McDonald, J. Mailloux, M. Mantsinen, A. Messiaen, A. Murari, J. Ongena, F. Orsitto, V. Pericoli-Ridolfini, M. Riva, J. Sanchez, F. Sartori, O. Sauter, A.C.C. Sips, T. Tala, A. Tuccillo, D. Van Ester, K-D. Zastrow, M. Zerbini, and contributors to the JET EFDA Programme, "Integrated scenario in JET using real-time profile control," *Plasma Phys. Contr. Fusion*, vol. 45, no. 12A, p. A367, 2003.

[76] T. Tala, L. Laborde, D. Mazon, D. Moreau, G. Corrigan, F. Crisanti, X. Garbet, D. Heading, E. Joffrin, X. Litaudon, V. Parail, A. Salmi, and contributors to the EFDA-JET workprogramme, "Predictive transport simulations of real-time profile control in JET advanced tokamak plasmas," *Nucl. Fusion*, vol. 45, no. 9, p. 1027, 2005.